*Journal of Structural Dynamics*, 2, (pp. 1-23) 2023
Experimental validation of impact energy scattering as concept for mitigating resonant vibrations

Journal of Structural Dynamics

CC BY

# Experimental validation of impact energy scattering as concept for mitigating resonant vibrations

Timo Theurich[1] and Malte Krack *[1]

[1] *University of Stuttgart, Pfaffenwaldring 6, 70569 Stuttgart, Germany*

## Abstract

The Vibro-Impact Nonlinear Energy Sink (or impact damper) is well-known for its ability to engage into transient resonance captures with arbitrary frequencies and thus has inherent broad-band effectiveness. Its working principle relies on (recurrent) energy localization and local dissipation within the contact region. Dissipative (inelastic) collisions are inevitably associated with damage and challenging to predict. Recently, it has been shown theoretically that the device is effective even for purely elastic collisions when the energy is (almost) irreversibly transferred from the critical low-frequency modes to high frequencies. In that case, the device is more properly termed Impact Energy Scatterer (IES). In the present work, we experimentally validate, for the first time, the working principle of the IES. To this end, we design a test rig consisting of a cantilevered beam, hosting a spherical impactor inside a cavity at its tip. The resonant vibrations of the lowest-frequency bending mode are reduced by a factor of 10-20. Given that the IES weighs less than $1\%$ of the host structure, this corresponds to a paramount vibration mitigation capability. We achieve excellent agreement between the measurements and the numerical predictions obtained by modeling the impacts as perfectly elastic. We also demonstrate that the dissipation in the contact region is negligible, while a substantial amount of energy is scattered to higher frequencies, validating the theoretically proposed working principle.

**Keywords:** impact damper; impact absorber; vibro-impact nonlinear energy sink (VI-NES); targeted energy transfer; inter-modal energy transfer; passive vibration mitigation

*Received on October 10, 2022*, *Accepted on January 10, 2023*, *Published on January 17, 2023*

## 1 Introduction

A Nonlinear Energy Sink (NES) is a means of passive vibration mitigation. It consists of a small mass attached to the host structure, whose vibrations are to be mitigated [1]. The attachment is designed to have no linear component (essential nonlinearity). The working principle of the NES is to localize and dissipate energy. The NES has no preferential frequency and can engage into resonance with arbitrary modes of the host structure over broad frequency ranges. This is an important benefit over tuned vibration absorbers, which are narrow-band devices. A practical challenge of the NES is to physically realize the essential nonlinearity of the attachment. The impact damper is a special kind of NES. Here, the essential nonlinearity is simply introduced by placing the additional mass freely into a casing of the host structure (Fig. 1b) and thus to let the mass undergo collisions with the host structure (free-play nonlinearity). While the impact damper dates back to the 1930s [2], the concept of the NES and the theoretical framework for their analysis was only recently developed [1]. The name Vibro-Impact Nonlinear Energy Sink (VI-NES) is now frequently used for the impact damper [1, 3, 4].

The NES theoretically has unlimited frequency bandwidth, the price for which is a limited (yet wide) amplitude range [1]. This is illustrated in Fig. 1a for the case of resonant excitation. At low excitation level, the nonlinearity is not

*krack@ila.uni-stuttgart.de

significantly activated so that the system responds as if the NES was not present. At high excitation level, the effective stiffness between NES and host structure becomes so large that their relative displacement becomes negligible, so that the NES just adds mass. This is true for most variants of the NES, including the common variant with a cubic-spring-type attachment and the VI-NES. In between these extreme cases, a strong vibration mitigation effect can be achieved. Two types of steady-state response are typical for resonantly-driven host structures with a NES: an almost periodic response where NES and host structure oscillate essentially in a synchronized way, and a strongly modulated response with repeated resonance captures where phases with synchronous oscillation alternate with phases with almost inactive NES [1]. One way to distinguish these response types is to determine the amplitude in every excitation period and calculate mean and maximum of those sequences. In the case of the strongly modulated response, mean and maximum amplitude show a large difference, while these values are close in the case of the almost periodic response. Depending on the excitation level, the resonant response occurs in either the almost periodic or the strongly modulated range. Interestingly, the point of optimum performance (minimum normalized resonant response) coincides in good approximation with the transition point: For slightly higher excitation level, the resonant response is almost periodic, while for slightly lower excitation level, the resonant response is strongly modulated. This is illustrated in Fig. 1a.

The impact damper relies on material dissipation in the contact region [5, 6, 7, 8, 9, 10, 11]. This is typically associated with inelastic deformation and damage. This might not be a critical point for seismic (shock) mitigation, where damage accumulates only sporadically, but it can be an important technical limitation for the case of resonant or self-excitation. The idea of the Impact Energy Scatterer (IES) is to avoid local dissipation in the contact region and instead exploit elastic impacts to transfer energy to higher-frequency modes. This is illustrated in Fig. 1b. Assuming the same inherent damping ratio for all modes, high-frequency modes dissipate energy more rapidly as they accumulate more vibration cycles within a given time span. Thus, the host structure's inherent damping (due to e. g. friction joints, distributed material and aerodynamic damping) is exploited more efficiently than in the case without IES. In this sense, the IES helps the structure to damp itself. This working principle was theoretically analyzed for systems under impulsive loading in [12], and, for the first time, for resonantly-driven vibrations in [13]. As the IES does not rely on local dissipation, it does not fall into the category of the NES. It is important to emphasize, however, that its behavior is virtually identical on the time scale of the resonantly-driven mode [14]. In particular, the ability to engage into transient resonance captures with arbitrary frequencies (inherent broad-band efficacy), the typical (strongly modulated vs. almost periodic) response regimes and the characteristic amplitude-dependence under periodic excitation, appear also for the IES. The main distinction between impact damper and IES is the cause of the dissipation (local dissipation in the contact region vs. irreversible energy scattering to higher-frequency modes). Exploiting energy scattering and avoiding local dissipation in the contact region has two major advantages of utmost technical relevance: First, damage is avoided. Second, the system behavior can be much better predicted since empirical laws to describe the local contact dissipation and plastic damage are not necessary. These aspects motivate the investigation and use of the IES, especially for flexible, e. g. lightweight/slender, host structures which are well-suited for inter-modal energy transfer via impacts.

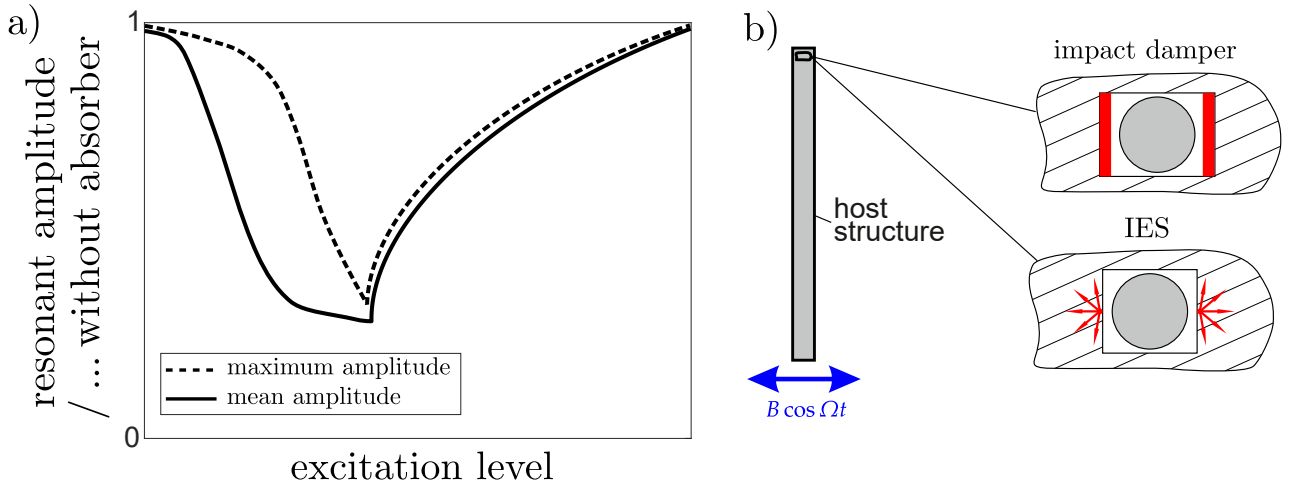


**Fig. 1:** (a) schematic illustration of the resonant response normalized by the response without absorber (NES, impact damper, or IES), as function of the excitation level and (b) schematic illustration of the difference between impact damper and IES.

It can be difficult to distinguish the theoretical concepts of impact damper and IES experimentally. We will use the term *impact absorber* to refer to the impact damper, the IES or any combination. Most research on impact absorbers has focused on host structures that can be well-described as single-degree-of-freedom systems (e. g. spring-mass oscillators). In this case, it can be shown that impact absorbers do not achieve any vibration mitigation unless the collisions are inelastic (dissipative) [13]. Consequently, analysis and design rely on dissipative contact laws involving empirical parameters. When those empirical parameters are properly set, good agreement between measurement and simulation can be achieved [15, 16, 17, 18, 19, 11, 20, 21, 22]. Some studies specifically design the impact absorber as a damper, e. g. by introducing viscoelastic material in the contact region [23, 24, 25]. Flexible host structures with impact absorbers were studied theoretically and confronted with experimental results in [26, 27, 28, 29, 23, 24, 30, 25, 31]. However, the analysis in all those studies relies on dissipative contact models. Typically, the empirical contact parameters are parameterized using a coefficient of restitution (assumed as known and fixed). Thus, the models are not qualified to make the distinction between impact damper and IES. The experimental work of Chabrier et al. [32] was apparently completed in parallel to ours; it also considers a beam with impact absorber and provides evidence of the contribution of higher-frequency modes.
It is the purpose of the present work to validate the concept of the IES for mitigating resonant vibrations experimentally, and to assess the predictive capabilities of the proposed computational approach. To this end, a test rig was designed to contain a cantilever beam as a host structure with a spherical IES[1] located at its tip, as described in Sect. 2. The numerical prediction approach is presented in Sect. 3. Based on tests without IES, the model of the host structure is updated and assessed in Sect. 4. Measurement results obtained for a large range of excitation levels and frequencies around the resonance with the lowest-frequency bending mode are confronted with numerical predictions in Sect. 5. The article ends with summary and conclusions in Sect. 6.

## 2 Design of the test rig

To experimentally analyze the vibration mitigation capabilities of the IES and to obtain a profound database for the validation of the numerical predictions, the test rig should meet the following requirements:

- The host structure should be reasonably flexible, have well-separated natural frequencies and kinematically simple mode shapes.
- The host structure should exhibit reasonably linear vibration behavior in a large range of amplitudes.

[1] In the following, we refer to the device already as IES, as it will be shown in the course of this work that this term is appropriate (damping within the contact region is shown to be negligible).

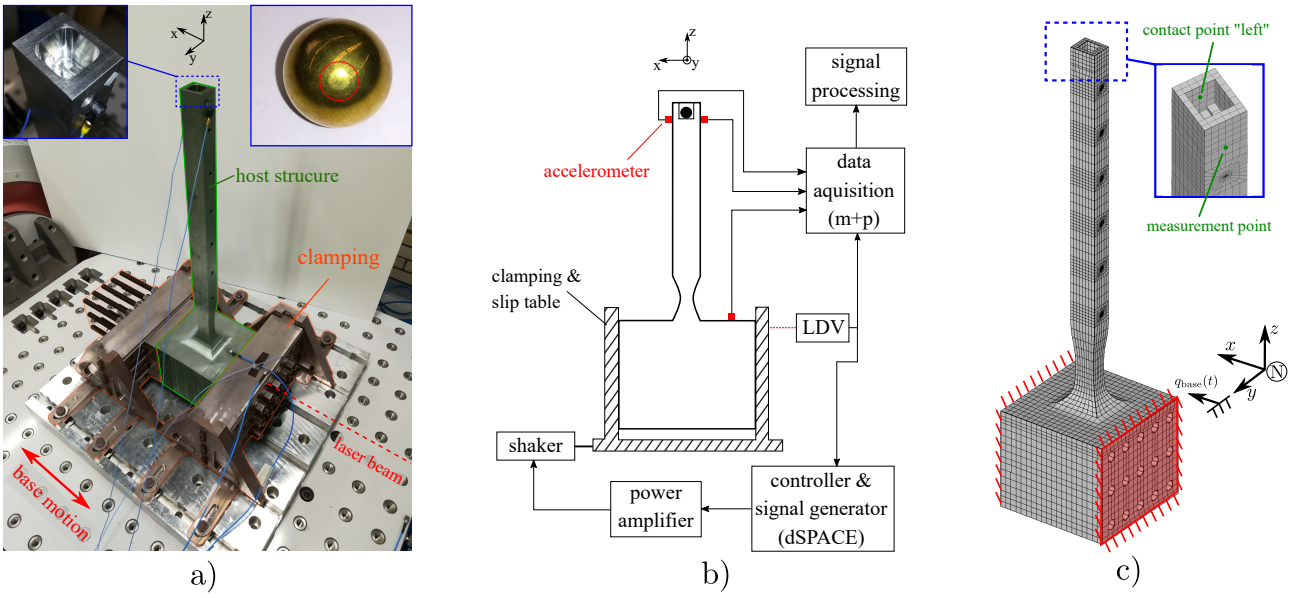


**Fig. 2:** Test rig: (a) photo, (b) schematic illustration including instrumentation, (c) finite element model of the host structure.

**Table 1:** Material properties

| Body (material) | Elastic modulus $E$ in GPa | Poisson's ratio $\nu$ | density $\rho$ in kg/m$^3$ |
|---|---|---|---|
| Host structure (steel) | $E_\mathrm{s}$ = 207 | $\nu_\mathrm{s}$ = 0.3 | $\rho_\mathrm{s}$ = 7,843 |
| IES (brass) | $E_\mathrm{a}$ = 102 | $\nu_\mathrm{a}$ = 0.3 | $\rho_\mathrm{a}$ = 8,490 |

- The host structure should be only lightly damped.
- The contact with the IES should facilitate the initiation of elasto-dynamic waves, and impact-induced damage should be avoided.
- Detrimental exciter-structure interaction should be avoided.

The designed test rig is depicted in Fig. 2. The material properties are listed in Tab. 1. The host structure is a cantilevered steel beam with a free length of about $400\ \mathrm{mm}$. The main cross section is $28\ \mathrm{mm} \times 22\ \mathrm{mm}$ (width in $x$-direction $\times$ width in $y$-direction). Thus, the dimensions of the cross section are small compared to the length, leading to a reasonable bending flexibility. The rectangular cross section ensures kinematically simple mode shapes. The mode of interest is the lowest-frequency bending mode in $x$-direction. To separate the bending modes in $x$- and $y$-direction, the characteristic neck close to the clamping was introduced. With this, the bending modes in the $y$-direction have lower frequencies than the corresponding ones in the $x$-direction. At the lower end, the beam extends to a massive block ($120\ \mathrm{mm} \times 120\ \mathrm{mm} \times 120\ \mathrm{mm}$), which is fixed via bolts to the clamping construction. The purpose of the massive block is to reduce the influence of the inevitable friction joints at the clamping, in order to achieve low damping and weak nonlinearity (of the low-frequency dynamics of interest).
The IES consists of a sphere placed inside a cavity at the free end of the beam. In order to avoid additional joints (potential sources of unintended contact nonlinearity and uncertainty) and to facilitate the initiation of elasto-dynamic waves, no additional parts (such as a casing) are introduced. Clearly, the downside of this is that the contact interface on the side of the host structure cannot be exchanged. To reduce the risk of severely damaging the cavity walls, the sphere is made of a softer material, namely brass. The nominal radius of the sphere is $R_\mathrm{a} = 7.92\ \mathrm{mm}$ (diameter $15.84\ \mathrm{mm}$). With this, the sphere weighs $17.7\ \mathrm{g}$, which corresponds to only about $1\%$ of the host structure (free length of beam without block), and to a modal mass ratio of $3.6\%$. The cavity dimensions are $17\ \mathrm{mm} \times 16.4\ \mathrm{mm} \times 16.9\ \mathrm{mm}$ ($x \times y \times z$). The cavity floor features a groove with a depth of $2\ \mathrm{mm}$ and a width of $8\ \mathrm{mm}$, which serves as a lateral guide for the sphere.
The test rig is mounted onto the slip table of a large electrodynamic shaker (TIRA TV 51010/LS-340, $11\ \mathrm{kN}$ nominal sine force), as indicated in Fig. 2a. The acceleration response was measured near the beam's tip and the base velocity was measured at the clamping via a Laser-Doppler vibrometer (LDV, Polytec OFV-5000). m + p VibRunner was used for data acquisition and signal post-processing was performed in MATLAB. The sampling rate for the frequency response tests was $51.2\ \mathrm{kHz}$. This is enough to have at least $400$ samples per fundamental excitation period in the stepped sine tests, and it is more than twice the highest relevant frequency of about $20\ \mathrm{kHz}$ (see Sect. 3.1). By using base excitation in the described way, one obtains a relatively small ratio between the mass of the flexible host structure (free length of beam, ca. 1.8 kg) and the total moving mass (shaker armature, slip table, clamping, block, beam; ca. 130 kg in total) of about $1.4\%$. This reduces detrimental exciter-structure interaction. Throughout the stepped sine tests, the base displacement was in good approximation harmonic. The excitation level was kept within tight bounds using a feedback controller implemented on a dSPACE MicroLabBox. More specifically, the fundamental Fourier coefficient of the measured base velocity was determined in real time using synchronous detection (see e. g. [33]) and a PI controller (parameters heuristically set to $K_\mathrm{p} = 700\ \mathrm{Vm^{-1}s}$, $K_\mathrm{i} = 600\ \mathrm{Vm^{-1}}$) was used to adjust the amplitude of the sinusoidal voltage input to the power amplifier of the shaker until the specified target excitation level is reached.

# 3 Numerical prediction approach

First, the mathematical model is described in Subsect. 3.1. Then, the numerical simulation approach is described in Subsect. 3.2.

## 3.1 Mathematical model

The host structure is modeled using finite elements with subsequent modal reduction, and the IES is modeled as a mass with a single degree of freedom (translation in $x$-direction) undergoing Hertzian-type contact with the host

structure. Details of this modeling approach are described in the following.
First, a finite element (FE) model is constructed from the designed geometry using the FE tool CalculiX [34]. The mesh is depicted in Fig. 2c. It consists of $10,176$ hexahedral elements with quadratic shape functions (C3D20) and a total of $52,214$ nodes. A homogeneous material (steel) with isotropic linear-elastic behavior is assumed, with the material properties listed in Tab. 1. The mesh should be fine enough to properly resolve the propagating waves within the structure due to the impacts. As a rule of thumb for wave propagation, the shortest relevant wave length should be sampled with at least 20 nodes [35]. The minimum wave speed in a homogenous elastic medium is that of transversal waves [36]:

$$c_\mathrm{T} = \sqrt{\frac{E_\mathrm{s}}{2(1+\nu_\mathrm{s})\rho_\mathrm{s}}}\,. \tag{1}$$

We will see later that the highest relevant frequency is that of the 9-th bending mode of about $f_\mathrm{max} = 20\,\mathrm{kHz}$. This leads to a minimum wave length of $c_\mathrm{T}/f_\mathrm{max} = 160\,\mathrm{mm}$ for the used steel. Considering that the used (second-order) C3D20 elements have mid-side nodes, the element length should not exceed $16\,\mathrm{mm}$. In the used mesh, the largest element length is $10\,\mathrm{mm}$. Moreover, it has been verified that the modal properties of the relevant 9 lowest-frequency bending modes do not significantly change when the mesh is further refined. Finally, as will be shown in Appendix A, the predicted linear frequency response function is in excellent agreement with the measurements, which further confirms the model quality. It should be remarked that a refinement of the mesh near the contact location is not necessary, as the local elasticity of the contact region is accounted for in the (Hertzian-type) contact model.
The equations of motion of the system can be expressed as:

$$\boldsymbol{M}\ddot{\boldsymbol{q}}_\mathrm{s} + \boldsymbol{K}\boldsymbol{q}_\mathrm{s} + \boldsymbol{w}_\mathrm{l} f_\mathrm{c,l} + \boldsymbol{w}_\mathrm{r} f_\mathrm{c,r} = -\boldsymbol{M}\boldsymbol{b}\ddot{q}_\mathrm{base}(t)\,, \tag{2}$$

$$m_\mathrm{a}\ddot{q}_\mathrm{a} - f_\mathrm{c,l} - f_\mathrm{c,r} = 0\,. \tag{3}$$

Herein, $\boldsymbol{q}_\mathrm{s}$ is the vector of nodal displacement degrees of freedom of the host structure, $\boldsymbol{M}$ and $\boldsymbol{K}$ are the corresponding symmetric and positive definite mass and stiffness matrices, respectively, and $q_\mathrm{a}$ and $m_\mathrm{a}$ are the $x$-displacement and the mass of the IES. Overdot denotes derivative with respect to time $t$. $f_\mathrm{c,l}$ and $f_\mathrm{c,r}$ are the normal contact forces between IES and host structure acting at the left and right cavity walls, respectively (as labelled in Fig. 2c). The vectors $\boldsymbol{w}_\mathrm{l}$ and $\boldsymbol{w}_\mathrm{r}$ describe the corresponding force directions in the coordinate system of the host structure (signed unity vectors if the coordinate system is accordingly aligned). The host structure is subjected to base excitation. More specifically, the faces highlighted in Fig. 2c are assumed to undergo the imposed displacement $q_\mathrm{base}(t)$ in the $x$-direction (sinusoidal with imposed frequency and controlled amplitude $a_\mathrm{base}$). The displacement vector $\boldsymbol{q}_\mathrm{s}$ counts relative to this imposed motion; the absolute displacement is $\boldsymbol{q}_\mathrm{s} + \boldsymbol{b}q_\mathrm{base}$, where $\boldsymbol{b}$ is a Boolean vector having value one in all entries corresponding to the $x$-direction and value zero otherwise. Accordingly, the matrices $\boldsymbol{M}$, $\boldsymbol{K}$ pertain to the clamped configuration (faces highlighted in Fig. 2c fixed).
The IES is assumed to move only in the $x$-direction. All other degrees of freedom are regarded as constrained. This seems well-justified by the lateral guide and the uni-axial excitation. Further, the IES is assumed to slide without friction. It was verified that the acceleration of the casing is much larger than the gravitational acceleration under a wide range of excitation conditions. This implies that the acceleration/deceleration due to friction forces is negligible in those ranges. Under relatively small excitation, friction can become relevant and this is analyzed separately in Appendix C. This is also supported by the observations in [37], where a spring-mass-oscillator equipped with a spherical impact damper was studied, and it was concluded that the friction coefficient has an important influence at low excitation/response levels only.
The main working hypothesis of the present paper is that immediate dissipation in the contact region is not needed to explain the working principle of the IES. Although clear marks of local plastic deformation were observed (see Fig. 2a-top-right or Subsect. 4.1), it is assumed that the by far largest part of the vibration mitigation effect is due to energy scattering. Consequently, the behavior in the contact region is modeled as linear-elastic. It is further assumed that the dimensions of the contact area remain small compared to the dimensions of the impacting bodies, so that half space theory is applicable. For the particular scenario of a sphere in contact with a flat wall, classical Hertzian theory holds. The normal contact forces are expressed as:

$$f_\mathrm{c,l} = k_\mathrm{H}\begin{cases}|\delta_\mathrm{l}|^{3/2} & \text{for } \delta_\mathrm{l} > 0, \text{ i. e. left contact closed}\\ 0 & \text{otherwise,}\end{cases}$$

$$f_\mathrm{c,r} = k_\mathrm{H}\begin{cases}-|\delta_\mathrm{r}|^{3/2} & \text{for } \delta_\mathrm{r} < 0, \text{ i. e. right contact closed}\\ 0 & \text{otherwise.}\end{cases} \tag{4}$$

Herein, $\delta_\mathrm{l}$ and $\delta_\mathrm{r}$ are the normal indentation at the left and right cavity wall, respectively, and $k_\mathrm{H}$ is the Hertzian spring constant (defined later). The indentation is defined as

$$\delta_\mathrm{l} = q_\mathrm{c,l} - q_\mathrm{a} - g, \tag{5}$$

$$\delta_\mathrm{r} = q_\mathrm{c,r} - q_\mathrm{a} + g, \tag{6}$$

where $q_\mathrm{c,l}$ and $q_\mathrm{c,r}$ are the $x$-displacement of the host structure at the left and right cavity wall, and $g$ is the clearance. The clearance is defined as the shortest distance between IES and either cavity wall, when the IES is placed in the middle between the cavity walls. $q_\mathrm{a}$, $q_\mathrm{c,l}$ and $q_\mathrm{c,r}$ are absolute displacements (counted from the inertial frame of reference), where $q_\mathrm{c,l} = \boldsymbol{w}_\mathrm{l}^\mathrm{T}\boldsymbol{q}_\mathrm{s} + q_\mathrm{base}$ and $q_\mathrm{c,r} = \boldsymbol{w}_\mathrm{r}^\mathrm{T}\boldsymbol{q}_\mathrm{s} + q_\mathrm{base}$.

Modal truncation is applied to Eq. 2. Thus, the nodal coordinates of the host structure are expressed as $\boldsymbol{q}_\mathrm{s} \approx \sum_{j=1}^{N_\mathrm{m}} \boldsymbol{\varphi}_j s_j$ using the mass-normalized mode shapes $\boldsymbol{\varphi}_j$ of the system without IES. Modal truncation yields a reduced model of the dynamics of the host structure:

$$\ddot{s}_j + 2D_j\omega_j\dot{s}_j + \omega_j^2 s_j + \boldsymbol{\varphi}_j^\mathrm{T}\boldsymbol{w}_\mathrm{l}f_\mathrm{c,l} + \boldsymbol{\varphi}_j^\mathrm{T}\boldsymbol{w}_\mathrm{r}f_\mathrm{c,r} = -\boldsymbol{\varphi}_j^\mathrm{T}\boldsymbol{M}\boldsymbol{b}\ddot{q}_\mathrm{base}(t) \qquad j = 1, \ldots, N_\mathrm{m}\,. \tag{7}$$

Herein, $\omega_j$ is the natural angular frequency of mode $j$ (associated with the modal coordinate $s_j$), and we have added modal damping (damping ratio $D_j$). Based on a convergence study, it was deemed sufficient to retain only the $N_\mathrm{m} = 9$ lowest-frequency bending modes in the $x$-direction. The highest retained frequency, $\omega_9/(2\pi)$, is $19.8\ \mathrm{kHz}$.

### 3.2 Numerical simulation

For the numerical simulation, time step integration was applied to Eqs. 3 and 7, considering Eqs. 4 - 6. The third-order Bogacki-Shampine scheme (MATLAB's $\mathrm{ode3}$) was used, which is suited for stiff ordinary differential equations and provides reasonable accuracy during the phases with no active contact. A fixed time step $\Delta t = 2\pi/(15\omega_9)$ was specified. This way, the period of the highest-frequency mode is sampled with $15$ time levels, which was found to yield a reasonable compromise between accuracy and computational cost.

## 4 Testing of the host structure without IES and model updating

To ensure a meaningful validation of the vibration mitigation effect, it is crucial to have an accurate model of the baseline system (without IES). To this end, the host structure was first tested alone and the mathematical model was updated. Impact Hammer Modal Testing was used to update elastic modulus and modal damping ratios (Appendix A). Frequency response testing under sinusoidal base excitation was used to assess the linearity of the host structure (Appendix B). Those analyses are common practice and hence described in an appendix. In contrast, the identification of contact parameters is presented in the following, as the methodology is non-standard and crucial for the understanding of the present study.

### 4.1 Identification of contact parameters

The contact between a sphere and a flat surface is inherently associated with high stress concentration (nominal point contact). Local plastic deformation is practically inevitable for metal-to-metal contact, especially for the tested high excitation/vibration levels which lead to high-velocity impacts. This is well known, see e. g. [38] or more recent experimental studies [39, 40]. Consequently, a small crater is formed at both cavity walls of the host structure (Fig. 3a), and the sphere slightly flattens (mark indicated with red circle in Fig. 2a-top-right). Under cyclic loading, plastic hardening and shakedown occur, beyond which purely elastic material behavior is expected [39]. However, multiple marks on the sphere suggest that the contact location on the sphere is not always exactly the same. Thus, a small amount of ongoing plastic deformation on the side of the spherical IES can be expected.
As the concept of the IES is to avoid plastic deformation in the contact region, the described damage is an undesired yet inevitable side effect. The plastic deformation is not modeled and thus the resulting change of the contact properties becomes an uncertainty. An important purpose of the present work is to assess the *predictive capabilities* of the proposed computational approach. To acknowledge the predictive character, most numerical investigations are carried out with the nominal geometry (flat cavity walls, IES of ideal spherical shape), rather than the actual geometry obtained during/after testing. To quantify the uncertainty, the change of the contact properties due to plasticity is

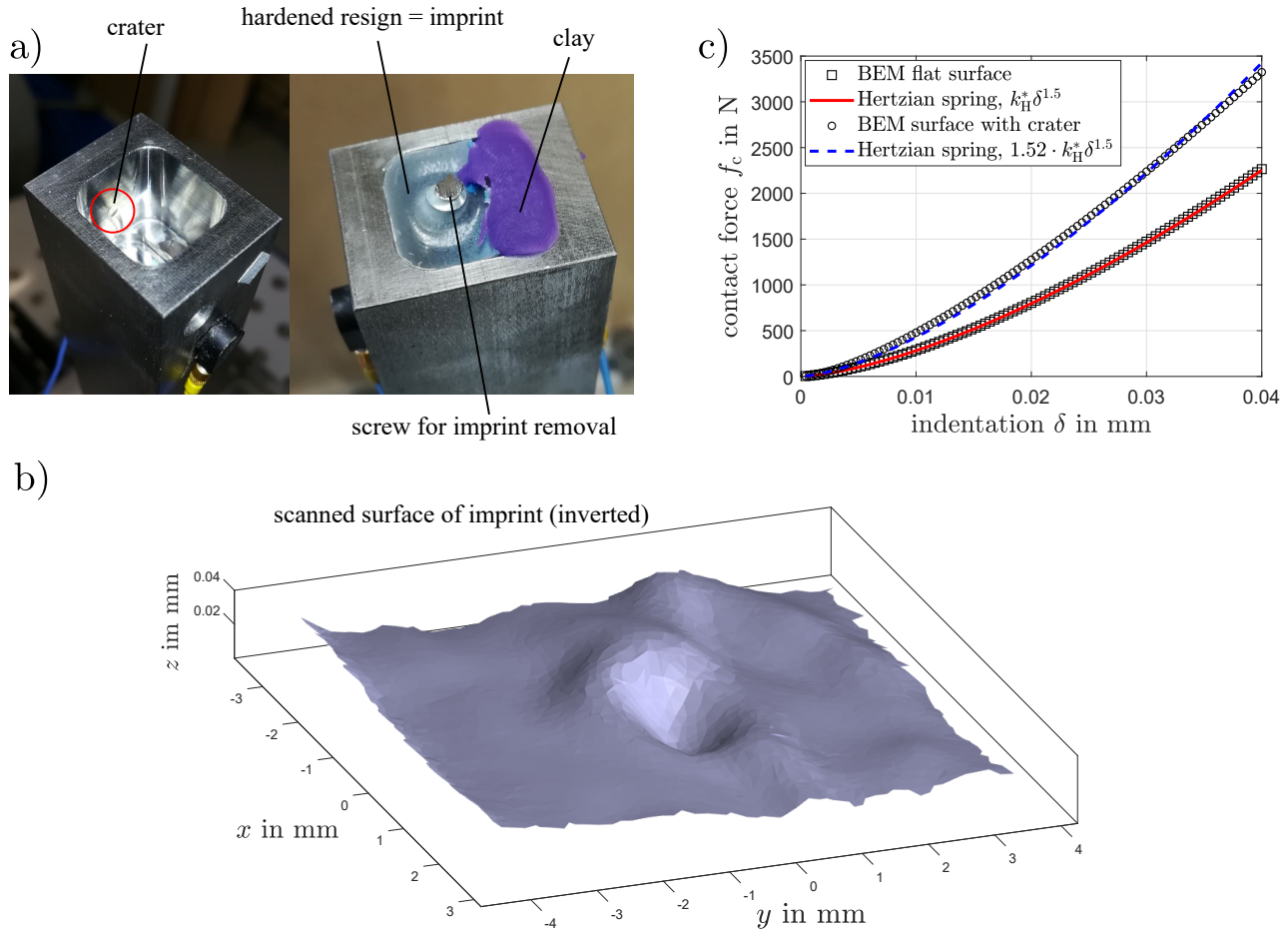


**Fig. 3:** Identification of contact parameters: (a) photograph indicating crater and preparation of its imprint, (b) inverted view of the scanned imprint surface, (c) contact normal force-indentation curve obtained by elastic half space theory.

estimated as described in the following, and the uncertainty propagation is analyzed separately.
To determine the actual geometry after testing, an imprint of the crater on the left cavity wall was made, and the flattening of the sphere was measured using a digital caliper. The imprint was made by filling half of the cavity with modeling clay and, thereafter, the other half with resin (see Fig. 3a). After the resin had hardened, the clay was removed and the imprint could be removed using a screw that was initially immersed in the fluid resin. The surface of the imprint was analyzed using a 3D surface scanner (GOM ATOS Compact Scan 5M). The scanned and inverted surface is shown in Fig. 3b. From the scanned surface it becomes evident that the material of the cavity wall has gradually been pushed to the sides (by the repeated impacts) to form elevations as well as an indentation with respect to the nominally flat part of the wall. The crater depth measured from the nominally flat part of the wall is $0.012$ mm. The sphere's diameter was determined to be $15.80$ mm in the flattened regions, which is slightly smaller than the nominal diameter $15.84$ mm of the unused sphere.
With the nominal diameter of the spherical IES, $2R_a = 15.84$ mm, and the nominal cavity width in $x$-direction, $17$ mm, the nominal clearance is $0.58$ mm. Due to the formation of the craters and the flattening of the sphere, the clearance is slightly enlarged by at most $0.012$ mm $+$ $0.02$ mm $=$ $0.032$ mm. Thus, the upper bound of the clearance is $0.58$ mm $+$ $0.032$ mm $=$ $0.612$ mm, as listed in Tab. 2.
Under the assumptions stated in Sect. 3.1, Hertzian theory applies. For the nominal scenario of a sphere with radius $R_a$ in contact with a flat surface, the Hertzian spring constant is

$$k_H^* = \frac{4}{3}\sqrt{R_a}\left(\frac{1-\nu_a^2}{E_a} + \frac{1-\nu_s^2}{E_s}\right)^{-1}, \tag{8}$$

where $E_a$, $\nu_a$ and $E_s$, $\nu_s$ are the elastic properties of the bodies in contact. Nominal parameters are labeled with an asterisk $(.)^*$ throughout this work. To consider the more complicated geometry depicted in Fig. 3b, a self-coded

boundary element solver (BEM) is used. It relies on the potential theory according to Boussinesq and Cerruti, see e. g. [41], valid for linear-elastic and isotropic half spaces subjected to surface loads only. This leads to a linear relationship between stresses and displacements at the surface. By using a regular two-dimensional mesh to discretize the surfaces, the elements of the corresponding coefficient matrix can be expressed in closed form [42]. Frictionless unilateral contact (Signorini conditions) is modeled and the resulting linear complementarity problem is solved using an Augmented Lagrangian scheme in conjunction with Jacobi relaxation. The resulting normal force-indentation curve is depicted in Fig. 3c. The indentation of $0.04\ \mathrm{mm}$ corresponds to the maximum obtained throughout the numerical simulations. Apparently, the force-indentation curve is steeper than in the case of a flat cavity wall: The plastic formation of the crater makes the contact stiffer/harder. A fit of a Hertzian-type law, $f_\mathrm{c} = k_\mathrm{H}\delta^{1.5}$, to the computed force-indentation curve is also shown in Fig. 3c. Due to the excellent agreement, we conclude that the Hertzian-type law is still a good approximation in the case of the more complicated contact geometry (crater), and that merely the Hertzian spring constant needs to be re-calibrated. For the depicted case, the effective Hertzian spring constant is $52\%$ larger than in the case of a flat cavity wall (obtained from Eq. 8). Here, it should be remarked that the IES was modeled as an ideal sphere to obtain the results shown in Fig. 3c. However, the actual geometry of the IES is not an ideal sphere but it is slightly flattened. Also, the measured crater corresponds to only the final geometry after the tests, whereas the actual geometry is time-variant during the test. For this reason, the value $k_\mathrm{H} = 1.52k_\mathrm{H}^*$ is viewed as an upper bound for the Hertzian spring constant. The *best estimate* is defined as an intermediate value, $k_\mathrm{H} = 1.25k_\mathrm{H}^*$.

### 4.2 Overview of nominal parameters and uncertainty bounds

The nominal values and uncertainty bounds of the contact parameters (clearance $g$ and stiffness $k_\mathrm{H}$) are listed in Tab. 2. The corresponding values for the modal frequency and damping ratio were determined as described in Appendix B and are also listed in this table. As stated above, most predictions (Sect. 5.1 to 5.3) were done with the nominal parameter values, $D^*, g^*, k_\mathrm{H}^*$, but the best estimate will be used as part of the uncertainty quantification (Sect. 5.4).

## 5 Testing of the host structure with IES

The purpose of the present section is to experimentally analyze the working principle and the vibration mitigation capability of the IES, and to validate the prediction approach. To this end, the IES is added to the host structure and the system is exposed to base excitation near the primary resonance with the lowest-frequency bending mode in the $x$-direction. The steady-state response to stepped sine excitation is analyzed in a wide range of excitation levels.
First, representative steady-state regimes of almost periodic and strongly modulated response (SMR) are shown in Subsect. 5.1. This permits to illustrate the challenges associated with the non-periodic character of the response and to describe how these were met in the simulation and in the experiment. Second, representative frequency responses at different excitation levels are shown in Subsect. 5.2. Third, a complete overview of the resonant response level vs. excitation level is given in Subsect. 5.3. Overall, very good agreement is achieved between simulation and measurement. The cause of the discrepancies at low excitation level (dry friction) is further analyzed in Appendix C. The propagation of parameter uncertainties (contact stiffness/Hertzian spring constant, clearance, damping ratio without IES) is analyzed in Subsect. 5.4, with a focus on the range from optimal to high excitation levels. In Appendix D, the number of significant impacts per period and the modal coefficient of restitution are estimated experimentally and confronted with predictions. Finally, the energy scattered to higher-frequency modes is estimated and it is analyzed to what extent local dissipation in the contact region may contribute to the observed vibration mitigation in Subsect. 5.5.
Throughout the figures presented in this section, the vibration response is quantified in terms of the amplitude $a$ of the tip displacement $q_\mathrm{tip}$ of the host structure (relative to the imposed base motion). Throughout this work, the magnitude of the fundamental harmonic component is used as amplitude measure. The displacement is normalized

**Table 2:** Summary of nominal parameters and uncertainty bounds

| Parameter | nominal value | minimum value | maximum value |
|---|---|---|---|
| modal frequency $\omega_1/(2\pi)$ in Hz | 117.4 | – | – |
| modal damping ratio $D_1$ in % | 0.085% | 0.075% | 0.090% |
| clearance $g$ in mm | 0.580 | 0.580 (−0%) | 0.612 (+5.5%) |
| Hertzian spring constant $k_\mathrm{H}$ in $10^3\mathrm{N/mm}^{3/2}$ | 282 | 282 (−0%) | 428 (+52%) |

by the resonant steady-state response amplitude in the linear case without IES, $a^{\text{noabs}^*}$. This is approximated as $a^{\text{noabs}^*} = \varphi_{\text{tip}} \frac{\boldsymbol{\varphi}^{\text{T}} \boldsymbol{M} \boldsymbol{b} a_{\text{base}}}{2D^*}$ (assuming well-separated, lightly-damped modes). Herein, $\boldsymbol{\varphi}$ is the mass-normalized shape (resonant mode), and $\varphi_{\text{tip}}$ is the corresponding value at the measurement location near the beam's tip. Here and in the following, the index $(.)_1$ of the modal properties is omitted for brevity, as the present work is limited to excitation frequency range around the fundamental mode.

## 5.1 Representative time histories of almost periodic and strongly modulated response

Representative time histories of almost periodic and strongly modulated response are depicted in Fig. 4. These two types of response regimes are characteristic for systems with either NES [1] or IES [13]. More specifically, the response is chaotic in both regimes, as shown numerically [13] and experimentally [17], and this was confirmed throughout the simulations and measurements in the present work via Poincaré mappings (not shown for brevity). Measurement and simulation are in very good agreement in both cases. Clearly, the steady-state vibrations are not periodic.

To characterize the response level, we use a mean and a maximum amplitude, as indicated with solid and dashed horizontal lines, respectively, in Fig. 4. As mentioned before, in the case of the almost periodic response, mean and maximum amplitudes are much closer together than in the case of the strongly modulated response. It was found that a wait time of $3$ s and $15$ s is sufficient to reach a reasonably steady state in the case with IES and without, respectively. With the nominal resonance frequency of $117.4$ Hz, this corresponds to $352$ and $1,761$ nominal excitation periods, respectively. The transients are longer in the case without IES due to the lower effective damping in this case. In the case of the experiment, the wait time includes the transient dynamics of the controller. Throughout the tests, the excitation level was within $3\%$ of the target value at the end of the wait time. Concerning the hold time, it was found that $5$ s, corresponding to $587$ nominal excitation periods, are sufficient to obtain reasonable convergence

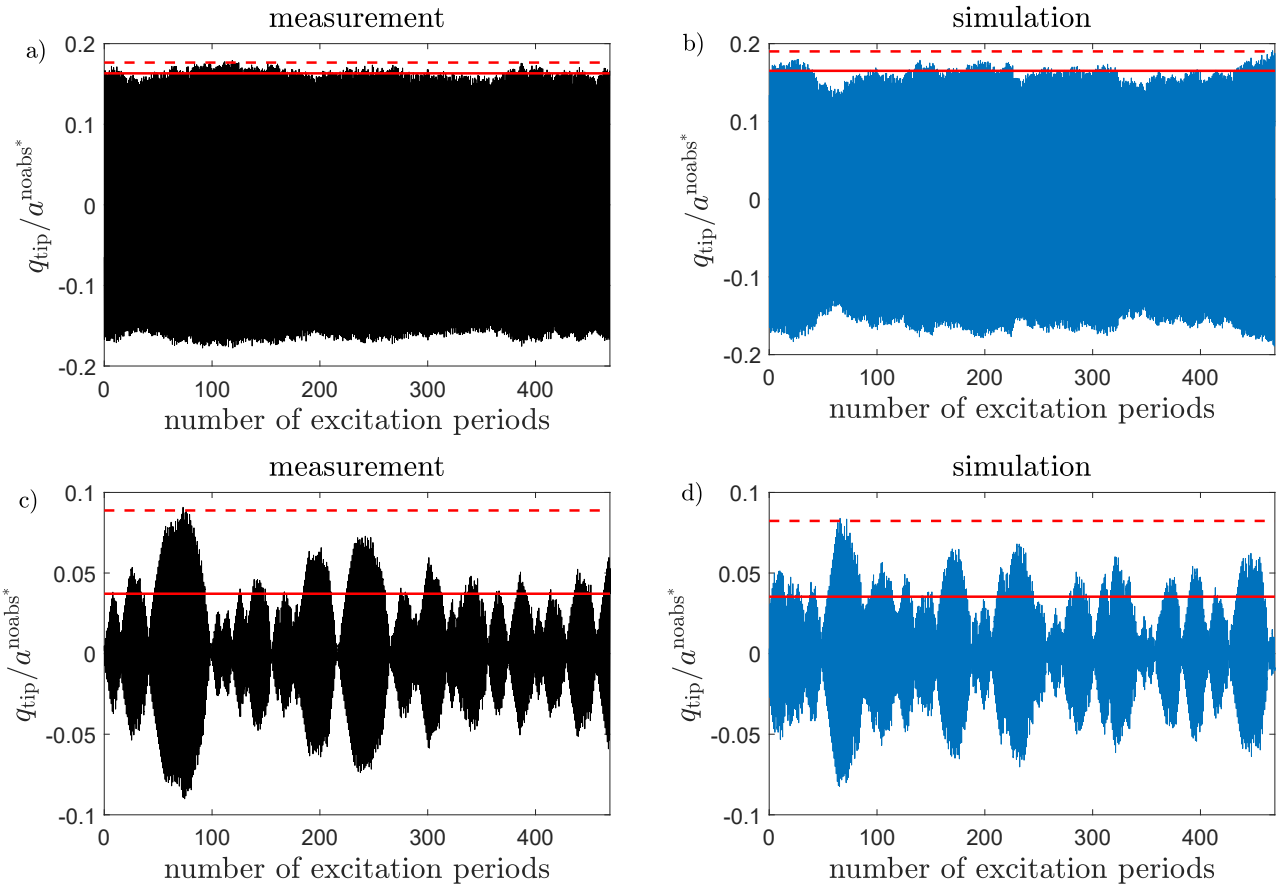


**Fig. 4:** Representative time histories illustrating the mean (solid) and the maximum (dashed) amplitude of the steady-state response at $a_{\text{base}}/a^*_{\text{base}} = 7.4$. Upper row: almost periodic response, $\eta = 0.976$; bottom row: strongly modulated response, $\eta = 0.99$; left: measurement; right: simulation. $a^{\text{noabs}^*}$ denotes the resonant steady-state response amplitude in the linear case without IES.

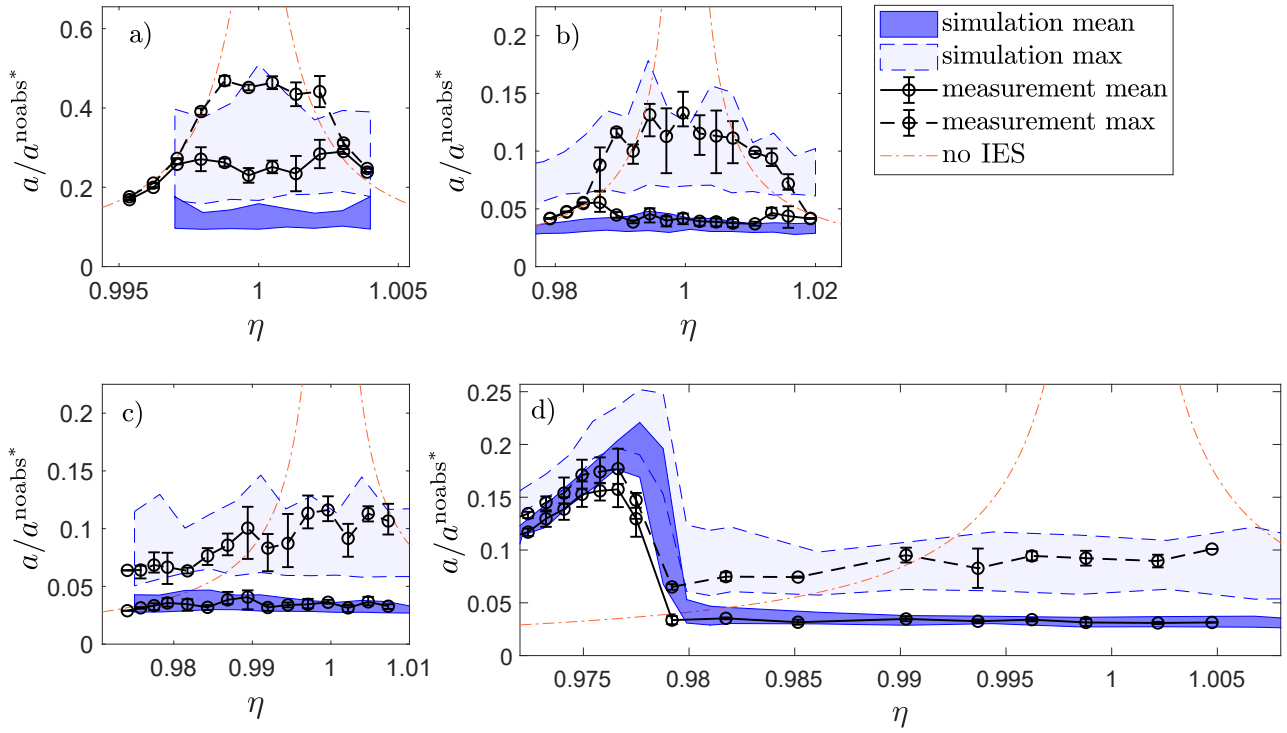


**Fig. 5:** Representative frequency responses at four different normalized excitation levels ( a) 1.26, b) 5.3 c) 6.7 d) 7.4, indicated also in Fig. 6). The repetition-induced variability of simulated and measured maximum and mean amplitudes was determined as described in Subsect. 5.1. $a^{\mathrm{noabs}^*}$ denotes the resonant steady-state response amplitude in the linear case without IES.

of the *mean amplitudes*. This applies to the largest range of excitation levels, both, in the case of almost periodic and in the case of strongly modulated responses. Only at the lowest excitation levels, where very long modulation cycles were observed, the hold time was tripled. As is well-known, it takes much longer to obtain convergence of the maximum than of the mean amplitudes. Indeed, the above defined hold times were not sufficient to obtain convergence of the *maximum amplitudes*. Based on the simulation, it was found that several tens of thousand excitation periods are required to obtain converged maxima. Taking into account that many excitation levels and frequencies must be measured, this would have led to prohibitive testing effort. Instead, it was accepted that the measurements do not yield a reliable estimate of the maximum amplitudes, and the described procedure leads to some repetition-variability. Thus, several repetitions were carried out, namely 3 (stepping the frequency up-down-up) at lower excitation levels and 5 (up-down-up-down-up) in the most interesting range of higher excitation levels. The spread obtained by those repetitions is depicted in the following figures. In the simulation, the same wait and hold times are used as in the measurement. To estimate the repetition-induced variability with the model, the simulations were repeated as well, starting at slightly different, randomly perturbed excitation frequencies in each stepped sine run (always with homogeneous initial conditions). Here, the number of repetitions was selected to ensure reasonable statistical convergence, which led to between 5 and 50 repetitions at high and low excitation levels, respectively.

## 5.2 Representative frequency responses

Fig. 5 shows representative frequency responses at different excitation levels. The excitation frequency is normalized by the nominal natural frequency, $\eta = \Omega/\omega^*$. The spreads (simulation) and the error bars (measurement) indicate the repetition-induced variability obtained as described in the previous subsection.
In wide ranges, the maximum amplitude is much larger than the mean, indicating strongly modulated response. At the higher excitation level depicted in Fig. 5d, a clear regime of almost periodic response can be seen in the range around $\eta = 0.975$. We define as *resonant response level* the largest response level reached in the excitation frequency range around the considered primary resonance. At the highest depicted excitation level (Fig. 5d), the resonant response level is reached in the almost periodic regime, while it is reached in the strongly modulated regime at the three depicted lower excitation levels (Fig. 5a-c). With the exception of the lowest excitation level (Fig. 5a), the measured response levels are largely within the predicted spread.

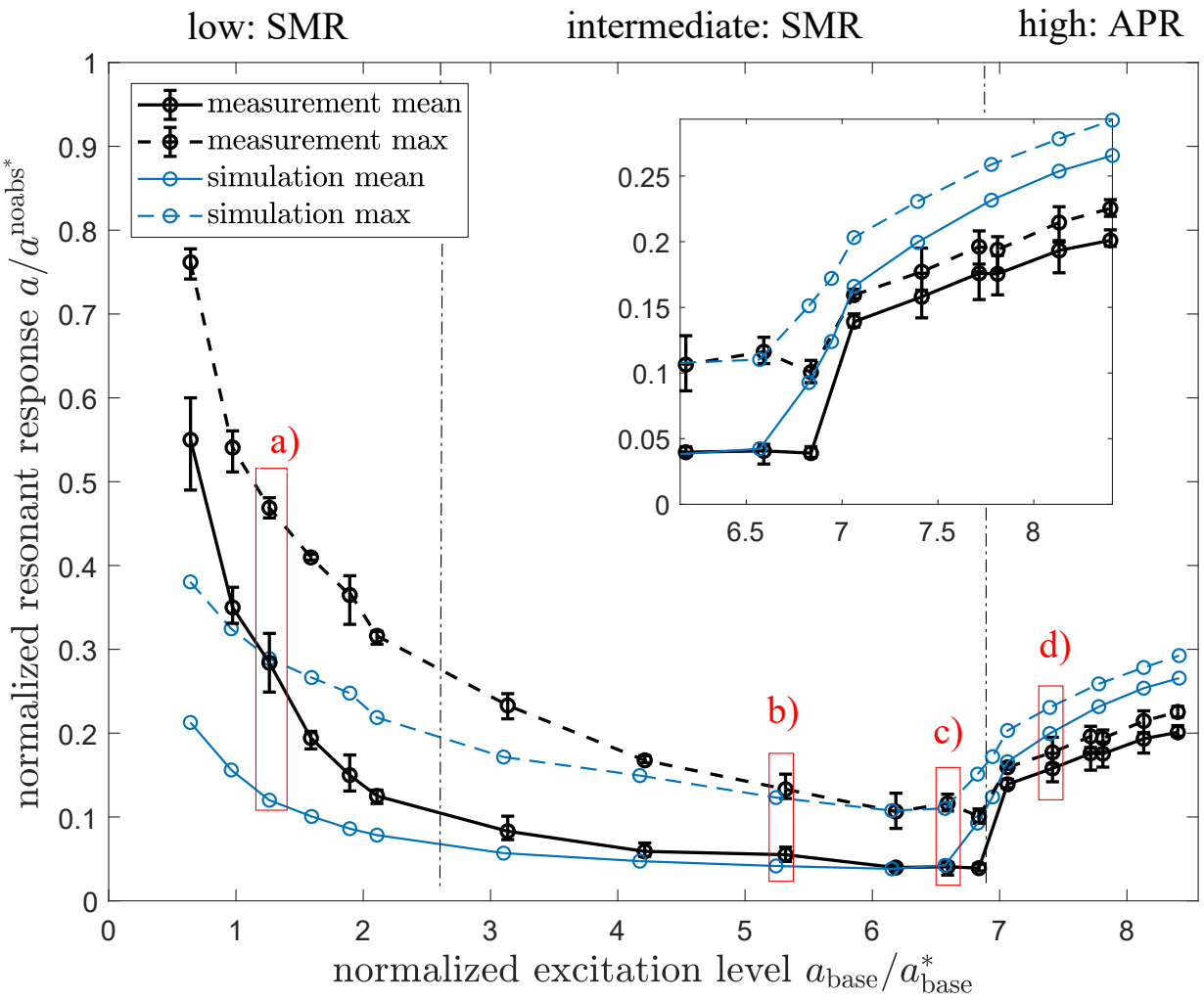


**Fig. 6:** Overview of the resonant response level as function of the excitation level. The boxes labelled with a)-d) correspond to the results shown in Fig. 5. Labels at the top indicate whether the resonant response level is reached in the almost periodic response (APR) or strongly modulated response (SMR) regime.

## 5.3 Overview: resonant response level vs. excitation level

An overview of the resonant response level vs. excitation level is given in Fig. 6. For clarity of the illustration, only average simulation results are plotted rather than the spreads in Fig. 5. It is also indicated in Fig. 6 whether the resonant response level is reached in the almost periodic response (APR) or strongly modulated response (SMR) regime.

The base excitation level is normalized by $a^*_{\mathrm{base}}$, which is defined as the level required to reach an amplitude equal to the clearance at the contact location. This is approximated using Eq. 7 as $a^*_{\mathrm{base}} = \frac{2D^*g^*}{\varphi_{\mathrm{c}}\boldsymbol{\varphi}^{\mathrm{T}}\boldsymbol{M}\boldsymbol{b}}$. Herein, $\varphi_{\mathrm{c}}$ is the value of the mass-normalized shape (resonant mode) at the contact location.

The excitation level leading to the strongest reduction of the resonant response level is at about $a_{\mathrm{base}}/a^*_{\mathrm{base}} \approx 6.7$ and will be referred to as *optimum* in the following. At the optimum, the maximum (mean) resonant response level is reduced by a factor of 10 (20). Given that the IES weighs less than $1\%$ of the flexible host structure, this corresponds to a paramount vibration mitigation capability.

The overall agreement of simulation and measurement is good. It is even excellent near the optimum, including the sharp transition of strongly modulated to almost periodic response. Some discrepancy is encountered at low excitation level. This is attributed to dry friction between the IES and the cavity walls (not modeled) and analyzed in Appendix C. Also, some discrepancy is encountered at high excitation level. This is mainly attributed to an increased contact stiffness (Hertzian spring constant $k_{\mathrm{H}}$) due to the plastic formation of a small crater at the left and right cavity walls and analyzed in Subsect. 5.4.

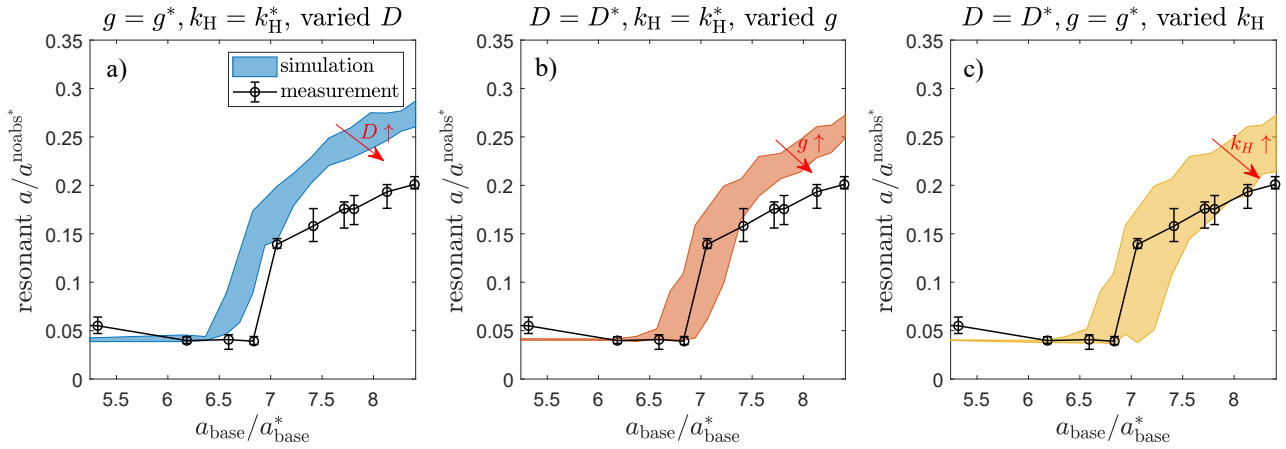


**Fig. 7:** Influence of uncertain parameters on the mean resonant response level near the optimum excitation level: Individual variation of (a) the modal damping ratio, (b) the clearance, (c) the contact stiffness.

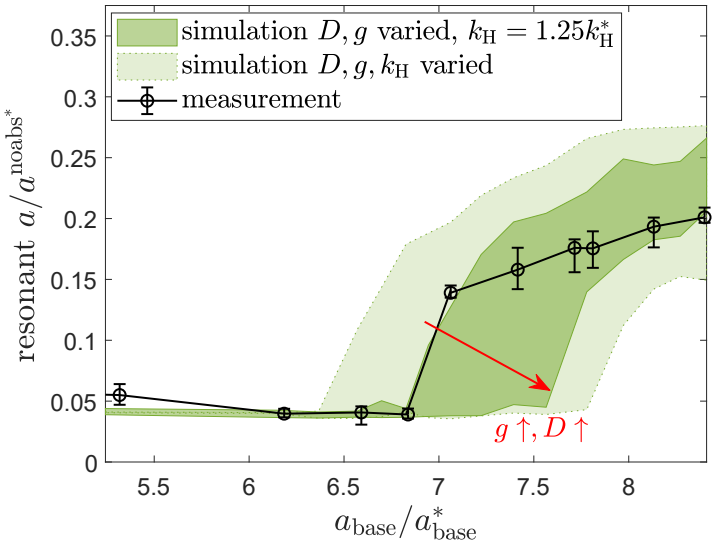


**Fig. 8:** Joint influence of all three uncertain parameters on the mean resonant response level near the optimum excitation level.

## 5.4 Uncertainty quantification

As established in Sect. 4, the modal damping ratio $D$, the clearance $g$ and the Hertzian spring stiffness $k_\mathrm{H}$ are uncertain model parameters. Recall that the clearance and the Hertzian spring stiffness alter due to the plastic deformation encountered during testing. So far, the nominal parameter values $D^*, g^*, k_\mathrm{H}^*$ have been used throughout the predictions, which means, in particular, that the plastic deformation was ignored and an ideal contact geometry (sphere on plane) was considered. We now investigate the influence of the uncertain parameters on the resonant response level, with a focus on the excitation level range near the optimum. To this end, the uncertainty bounds summarized in Tab. 2 are considered. The resulting simulation results are depicted as spreads in Figs. 7 and 8, and confronted with the measurements. To compute these spreads, it is exploited that the results are monotonous in the respective parameters, so that it is sufficient to consider only the interval limits of the uncertain parameters. The individual influence of each uncertain parameter ($D$, $g$ and $k_\mathrm{H}$) is illustrated in Fig. 7, while the joint influence is illustrated in Fig. 8. For clarity, only the mean resonant response level is illustrated.

Interestingly, the mean resonant response level in the strongly modulated regime is almost invariant under the variation of the uncertain parameters. In the almost periodic regime, a larger damping ratio leads to a lower response (Fig. 7a). A change in clearance mainly shifts the curve along the horizontal axis (Fig. 7b), which is in line with the theoretical results established in [14]. A higher contact stiffness increases the impact-induced energy scattering and thus reduces the resonant response level (Fig. 7c). Among the three parameters, the contact stiffness has the largest influence, not only because of the high sensitivity but also due to the large relative uncertainty of this parameter.

When the joint influence of all three uncertain parameters is considered, a rather large uncertainty spread of the response is obtained (light shaded area in Fig. 8). When the contact stiffness is fixed to the best estimate, $k_\mathrm{H} = 1.25k_\mathrm{H}^*$ (cf. Sect. 4.1), the measurements are largely within the residual uncertainty spread. Likely reasons for remaining deviations include the ongoing plastic deformation of the IES and the change of the material properties (in particular: hardening) within the contact regions.

## 5.5 Local dissipation in the contact region vs. energy scattering

The agreement between measured response and that predicted with a conservative contact law suggests that the observed vibration mitigation is caused by energy scattering. In this subsection, we first estimate the energy that is actually scattered to the higher-frequency modes. We then augment the conservative contact model by a damping element and analyze to what extent local dissipation in the contact region could contribute to the overall dissipation. To estimate the energy scattered to higher-frequency modes, we exploit that the system behaves in good approximation linearly between impacts. The impacts are detected in the experiment using the algorithm described in Appendix D. As explained there, the impact detection occasionally fails (especially when the impact occurs with too low velocity), so that the following investigation had to be limited to a relatively short section of the steady-state almost periodic resonant response. The results are presented for a representative excitation level $a_\mathrm{base}/a_\mathrm{base}^* = 7.4$ (depicted in Fig. 4a-b). In the linear case between two impacts, the tip displacement, $q_\mathrm{tip}$, can be expressed as the superposition of homogeneous and particular solution,

$$q_\mathrm{tip}(t) = \underbrace{\varphi_{\mathrm{tip},1}\left(A\cos(\Omega t) + B\sin(\Omega t)\right)}_{\text{particular solution}} + \underbrace{\sum_{j=1}^{N_\mathrm{m}} \varphi_{\mathrm{tip},j}\left(\alpha_j\cos(\omega_{\mathrm{d},j}t) + \beta_j\sin(\omega_{\mathrm{d},j}t)\right)\mathrm{e}^{-D_j\omega_j t}}_{\text{homogeneous solution}} . \tag{9}$$

Here, it is assumed that the particular solution is dominated by the resonant mode. The natural frequencies $\omega_j$, damping ratios $D_j$ and damped natural frequencies, $\omega_{\mathrm{d},j} = \omega_j\sqrt{1-D_j^2}$ are known from modal analysis. As before, we truncate to the $N_\mathrm{m} = 9$ lowest-frequency bending modes. The mass-normalized mode shapes $\varphi_{\mathrm{tip},j}$ at the beam's tip are adopted from the model. The coefficients $A,B,\alpha_j,\beta_j$ with $j = 1,\ldots,N_\mathrm{m}$ are unknown. These are estimated from the measured time series of the tip velocity via a least-squares fit of Eq. 9 (evaluated on velocity level). Figs. 9-10 show the simulated and the measured time section of the velocity, respectively, along with the reconstruction obtained via Eq. 9 using the estimated coefficients. The excellent agreement between reconstruction and reference indicates that the described procedure is able to accurately identify the modal contributions from the given time series. The instantaneous mechanical energy of each mode after an impact can be easily determined from the estimated coefficients. For the depicted time section of the simulation (measurement), it was determined that a fraction of $15\%$ ($12\%$) of the host structure's total mechanical energy is contained in the higher-frequency modes. On first sight, the rather low contribution of the high-frequency modes might seem contradictory to the proposed energy scattering phenomenon. It should be recalled that the energy is dissipated very rapidly in these modes, as there are many modal oscillation cycles between two impacts (e. g. in the almost periodic regime). This is why these modes do not accumulate substantial amount of energy. The slight deviation ($15\%$ vs. $12\%$) is attributed to the inherent variability of the almost periodic response. Due to the challenges encountered in the impact detection, the energy measures cannot be reliably determined over longer time sections from the measurements to further analyze this. Still, the experimental results show that a substantial portion of the energy is scattered to higher-frequency modes. Moreover, this portion is in good accordance with the prediction obtained using a purely elastic (non-dissipative) contact model. This provides further evidence that the observed vibration mitigation mainly relies on energy scattering rather than local dissipation in the contact region.

To further analyze to what extent local dissipation in the contact region could contribute to the overall vibration mitigation effect, we augment the contact model by damping. More specifically, we extend the conservative Herzian spring law according to the model proposed in [43]. For the left contact, this reads (cf. Eq. 4):

$$f_\mathrm{c,l} = \begin{cases} k_\mathrm{H}\left|\delta_\mathrm{l}\right|^{3/2} + d_\mathrm{H}\left|\dot{\delta}_\mathrm{l}\right| & \text{for } \dot{\delta}_\mathrm{l} > 0 \wedge \delta_\mathrm{l} > 0 \\ k_\mathrm{H}\left|\delta_\mathrm{l}\right|^{3/2} & \text{for } \dot{\delta}_\mathrm{l} < 0 \wedge \delta_\mathrm{l} > 0 \\ 0 & \text{otherwise}, \end{cases} \tag{10}$$

$$d_\mathrm{H} = 2\xi\sqrt{k_\mathrm{H}\sqrt{|\delta_\mathrm{l}|}\frac{m_\mathrm{beam}m_\mathrm{a}}{m_\mathrm{beam}+m_\mathrm{a}}}, \xi = \frac{9\sqrt{5}}{2}\frac{1-r_\mathrm{cont.diss.}^2}{r_\mathrm{cont.diss.}(r_\mathrm{cont.diss.}(9\pi-16)+16)} .$$

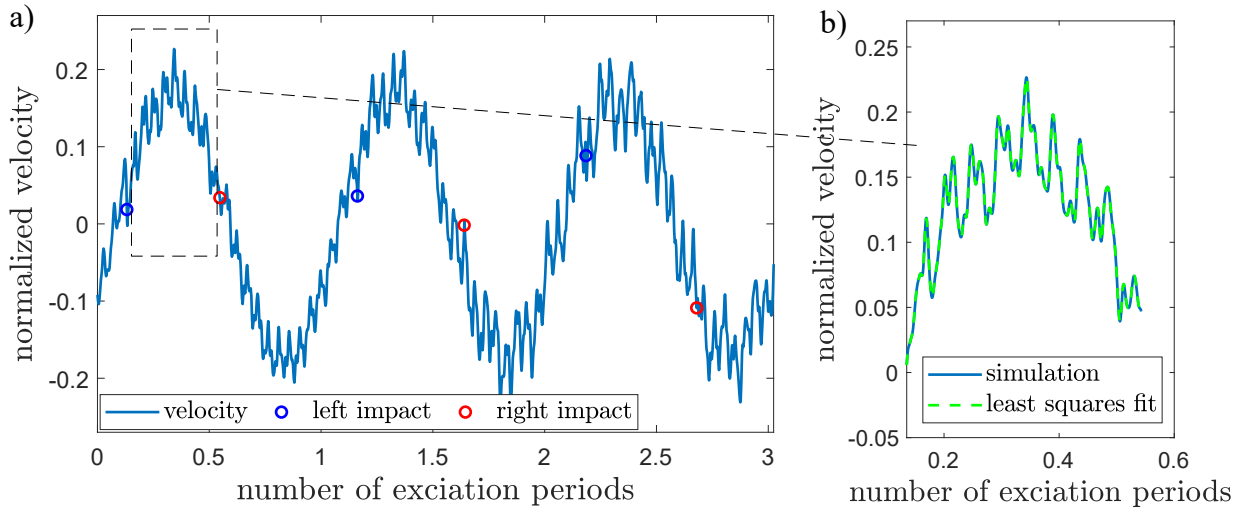


**Fig. 9:** Time interval of the *simulated* velocity near the beam's tip $\dot{q}_{\mathrm{tip}}$ for $a_{\mathrm{base}}/a^*_{\mathrm{base}} = 7.4$ and $\eta = 0.976$: (a) overview and indication of impact events; (b) comparison of reconstruction from least-squares fit of modal velocities against reference. All velocities are normalized with $\Omega a^{\mathrm{noabs}^*}$.

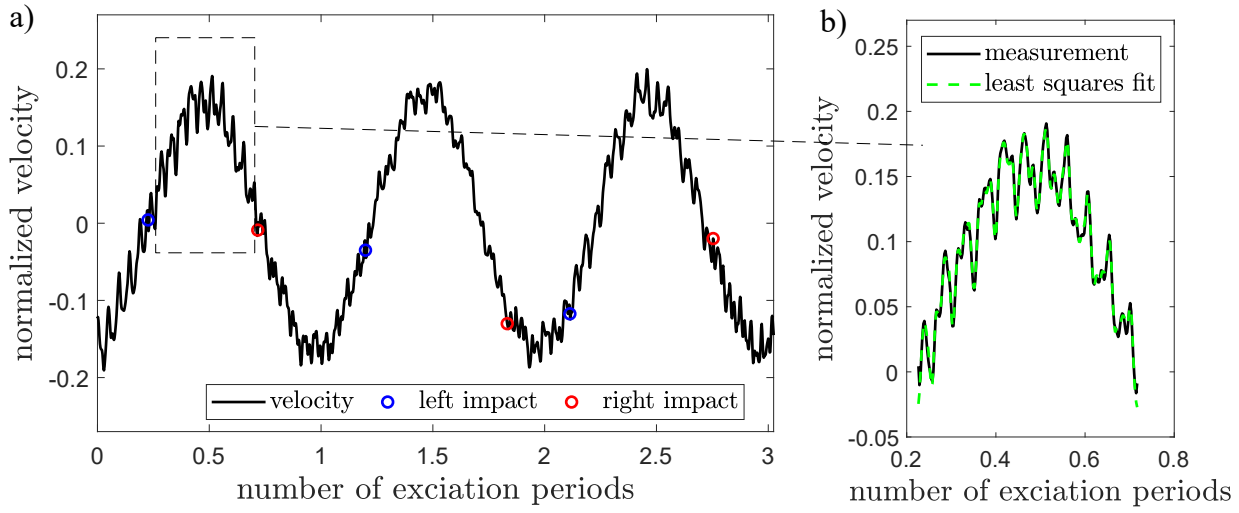


**Fig. 10:** Time interval of the *measured* velocity near the beam's tip $\dot{q}_{\mathrm{tip}}$ for $a_{\mathrm{base}}/a^*_{\mathrm{base}} = 7.4$ and $\eta = 0.976$: (a) overview and indication of impact events; (b) comparison of reconstruction from least-squares fit of modal velocities against reference. All velocities are normalized with $\Omega a^{\mathrm{noabs}^*}$.

The model of the right contact is extended analogously. The model introduces dissipation only in the approach phase ($\dot{\delta}_{\mathrm{l}} > 0$), but not in the restitution phase ($\dot{\delta}_{\mathrm{l}} < 0$). The damping coefficient $d_{\mathrm{H}}$ is parameterized using the mass of the IES, $m_{\mathrm{a}}$, the mass of the beam (free length without block), $m_{\mathrm{beam}}$, and a restitution coefficient $r_{\mathrm{cont.diss.}}$. $r_{\mathrm{cont.diss.}} = 1$ recovers the conservative Hertzian spring law, whereas $0 < r_{\mathrm{cont.diss.}} < 1$ models local dissipation in the contact region. The parameter $r_{\mathrm{cont.diss.}}$ was varied and the influence on the mean resonant response level near the optimum excitation level is shown in Fig. 11. Here, the contact stiffness was set to its best estimate, $k_{\mathrm{H}} = 1.25 k^*_{\mathrm{H}}$; damping and clearance are set to their nominal values $D^*, g^*$. The results indicate that local dissipation in the contact region may indeed play a certain role at high excitation levels, $a_{\mathrm{base}}/a^*_{\mathrm{base}} > 7.5$, and thus high impact velocities, as conjectured earlier. At lower excitation levels, and thus closer to the optimum excitation level, the dissipation in the contact region must be negligible. Even for $r_{\mathrm{cont.diss.}} = 0.99$, which seems realistic for higher excitation levels, merely $5\%$ of the supplied energy is dissipated in the contact region. This is less than the $10\%$ dissipated in the fundamental mode. The by far largest part, namely $85\%$, is dissipated in the higher-frequency modes (even though / because they only contribute with $15\%$ to the total mechanical energy). It is interesting to compare the value $r_{\mathrm{cont.diss.}} = 0.99$, which accounts for only the local dissipation in the contact region, with the effective coefficient of restitution $r$, which accounts also for the scattering, and is defined in Appendix D. As shown in the appendix, the value of $r$ is experimentally identified to

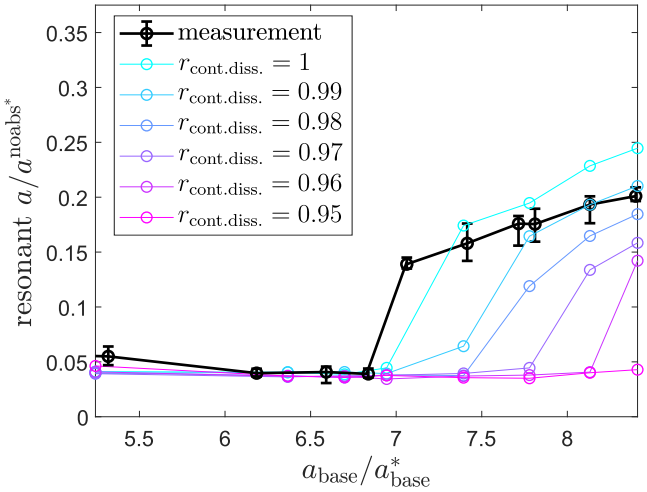


**Fig. 11:** Influence of additional local dissipation in the contact region on the resonant mean response. In all simulations, the contact stiffness is fixed to the best estimate and the damping and clearance are both set to their nominal value.

be about $0.8$, and this value is, again, in very good agreement with the predictions obtained using a conservative contact model. This clearly demonstrates that the spherical impactor acts primarily as an IES rather than as an impact damper.

# 6 Summary and conclusions

In this work, a test rig was designed to experimentally analyze the concept of the IES for mitigating resonant vibrations. For the predictions, the host structure was modeled using conventional modal truncation, and the contact with the spherical IES was described using a Hertzian-type contact model. Based on measurements without IES, the modal model was updated and it was found that the dynamics of the host structure alone can be well-approximated as linear in the relevant amplitude range. The impactor was then added to the host structure and the system was exposed to harmonic base excitation near primary resonance with the lowest-frequency bending mode. Excellent agreement between measurements and predictions was obtained, especially in the range near the optimum excitation level. The discrepancies at low excitation level were explained by dry friction (using a refined model). Slight discrepancies at high excitation level were explained by uncertainties in the modal damping ratio (slightly amplitude-dependent) and, more importantly, in the contact properties (clearance, contact stiffness). The latter changed due to plastic deformation leading to a slight flattening of the sphere and the formation of a small crater on both cavity walls. It was demonstrated that the local dissipation in the contact region is indeed negligible, and that the by far largest amount of the supplied energy is irreversibly scattered to the higher-frequency modes. This confirms that the impactor indeed acts as IES (rather than as an impact damper). The excellent agreement with the measurements indicates that the proposed prediction approach involving a purely elastic contact model is suitable to analyze and design flexible host structures with an IES, without the need to resort to an empirical coefficient of restitution.

# Authors' Contributions

Timo Theurich: research implementation; writing
Malte Krack: research concept; supervision; writing

# Acknowledgements

The authors would like to thank Dr. Christian Koch and Max Lorenz for assisting with the extraction of the crater's imprint surface and Daniel Fochler, Florian Müller and Roman Raabe for their advice on the BEM simulation, the measurement setup and the test rig design, respectively.

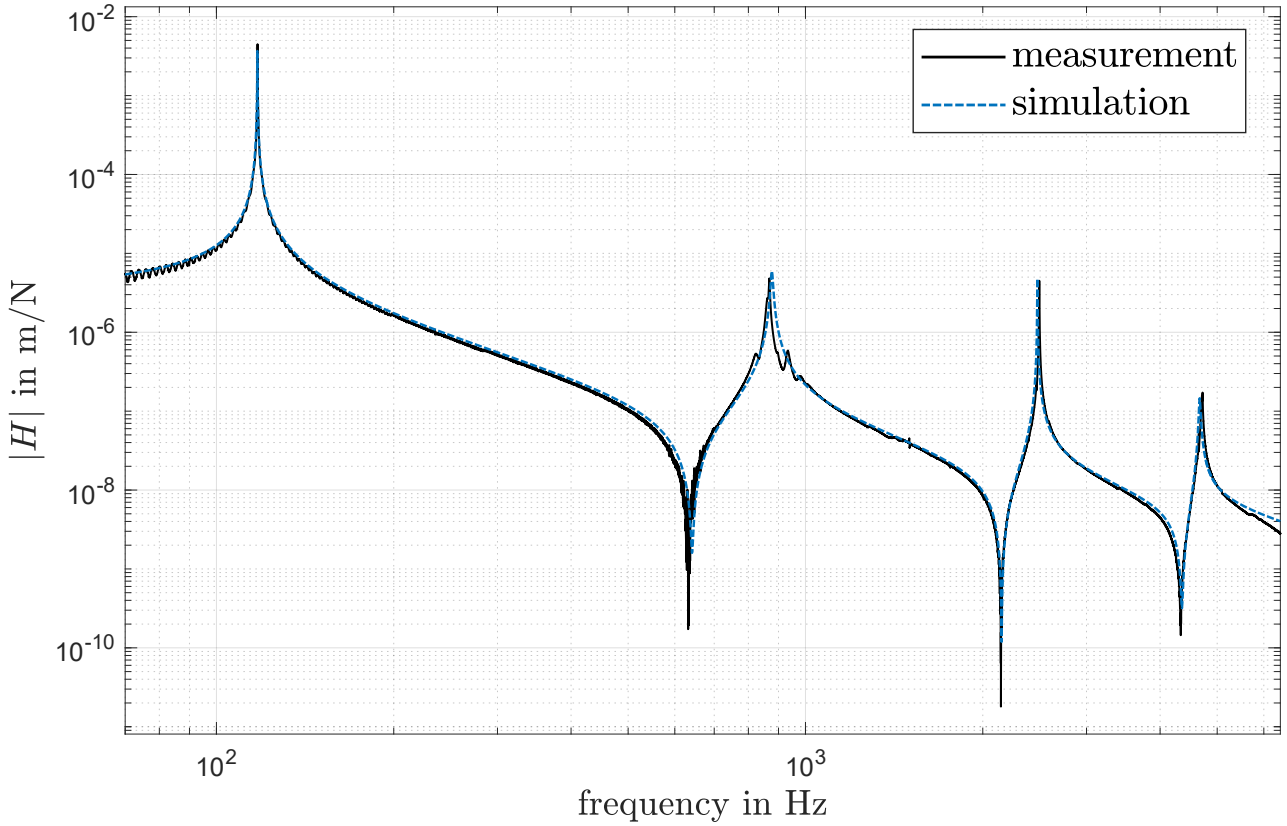


**Fig. A.1:** Linear frequency response function for force input slightly above the accelerometer at the beam's tip and displacement output on the opposing side (both in $x$-direction); estimate obtained using Impact Hammer Modal Testing vs. updated model.

# Appendix

## A Impact Hammer Modal Testing: Updating of elastic modulus and modal damping ratios

The force was applied to a point directly above the left accelerometer at the beam's tip, using a modal hammer (PCB 086C01). The impact was applied in the $x$-direction, and the response was measured at the accelerometer (PCB 352C22) on the opposing side (see Fig. 2). For the hammer tests, a sampling rate of $16.384$ kHz was used, so that the four lowest-frequency bending modes in the $x$-direction can be captured (highest useful frequency $6.4$ kHz). With the maximum block size of $2^{18}$ provided by the equipment, the sampling rate leads to a frequency resolution of $0.0625$ Hz, which was deemed sufficient in view of the very low damping of the structure. The hammer test was carried out six times. Subsequently, the $H_\mathrm{v}$ estimator of the frequency response function (geometric mean of $H_1$ and $H_2$ estimators [44]) was computed. The result is shown in Fig. A.1. To obtain the frequency response function (FRF) in terms of displacement, the measured acceleration was integrated in the frequency domain. From the FRF, the natural frequencies and modal damping ratios of the first four bending modes in the $x$-direction are obtained using conventional modal parameter identification, and the results are listed in Tab. 1.

**Table A.1:** Experimentally extracted linear modal frequencies and damping ratios of the first four bending modes in the $x$-direction; frequency errors of the updated model

| Mode | 1 | 2 | 3 | 4 |
|---|---|---|---|---|
| Frequency in Hz | 117.4 | 886 | $2,494$ | $4,712$ |
| (error of updated model) | (0.05%) | (1.4%) | (0.5%) | (0.7%) |
| Damping ratio in % | 0.06 | 0.44 | 0.05 | 0.31 |

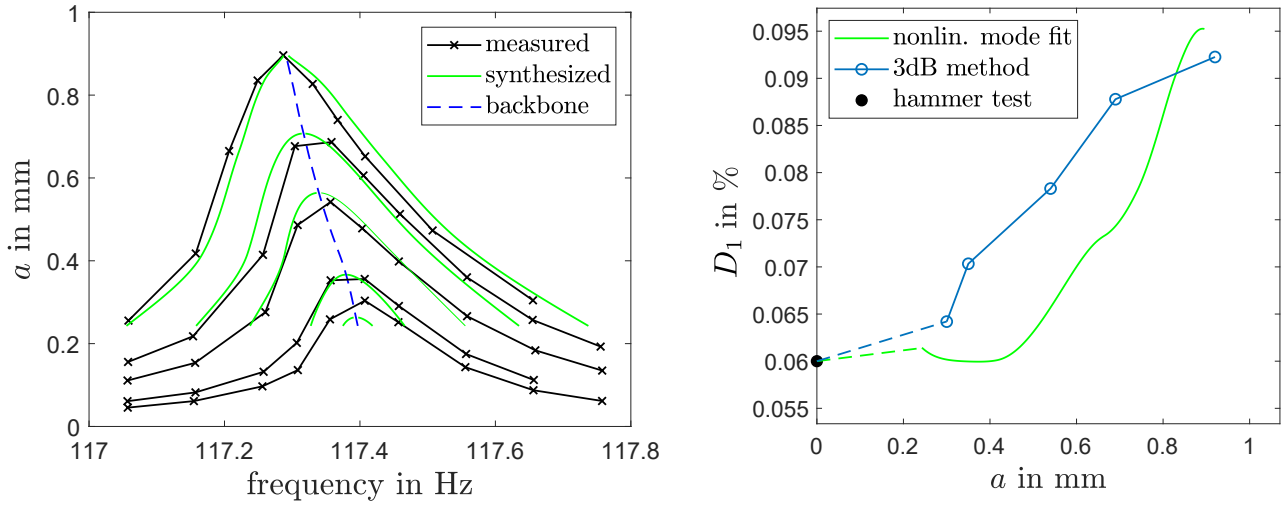


**Fig. B.1:** Response of the host structure without IES to stepped sine excitation of levels $a_{\text{base}} \in [2.0, 2.7, 4.7, 6.7, 9.4] \cdot 10^{-7}$m: (a) frequency response and (b) identified modal damping ratio vs. amplitude.

The elastic modulus of the host structure was updated from the value specified by the manufacturer, $210$ GPa, to a value of $207$ GPa, in order to better match the lowest-frequency mode. The elastic modulus of the IES, $E_{\text{a}}$, and the Poisson ratios, $\nu_{\text{s}}$, $\nu_{\text{a}}$ were selected according to manufacturer specifications. The mass density of the host structure, $\rho_{\text{s}}$, and that of the IES, $\rho_{\text{a}}$, were determined by weighing the bodies individually and considering the volume of the nominal geometry. The final material parameters are those listed in Tab. 1. The experimentally identified modal damping ratios, $D_1, \ldots, D_4$ are adopted in the model (Eq. 7). The remaining damping ratios, $D_5, \ldots, D_9$ were set to a value of $0.1\%$, which is close to the mean of $D_1, \ldots, D_4$. In line with the theoretical study in [14], the predicted results are largely robust with respect to the modal damping of the higher-frequency modes, as long as they are of a similar order of magnitude as the damping of the lower-frequency modes.
The natural frequencies of the updated model are in good agreement with the experimentally identified values (Tab. 1). Moreover, the linear FRF obtained from the updated model matches well the experimental estimate (Fig. A.1). Looking closely, a secondary peak can be identified in the measured FRF, slightly above the second-lowest resonance. This is attributed to the dynamics of the clamping (not modeled) and therefore has no counterpart in the results obtained from the model. Overall, it is concluded that the updated linear model of the host structure represents well the behavior in the absence of the IES up to at least $6.4$ kHz, and is therefore well-suited for the subsequent validation of the vibration mitigation effect.

# B Shaker Testing: Assessment of linearity

The vibration mitigation effect was analyzed in a relatively broad range of excitation levels. The corresponding resonant response level also spans a broad range. It is thus interesting to know to what degree the host structure (without IES) behaves linearly in this range. To analyze this, the host structure alone was exposed to stepped sine excitation of different levels near the primary resonance with the lowest-frequency bending mode in $x$-direction.
In Fig. B.2a, the frequency response of the host structure is depicted in terms of the amplitude $a$ of the tip displacement $q_{\text{tip}}$. A slight softening effect and a slight damping increase (widening of the resonance peak) can be seen in Fig. B.2a. This type of nonlinearity is typical for dry friction and it is attributed to the friction joints at the clamping. To quantify the damping ratio, two methods were employed, the half-power bandwidth method, and the fitting of a single-nonlinear-mode model (similar to [45]). Besides the amplitude-dependent damping illustrated in Fig. B.2b, the latter method also yields the backbone curve shown in Fig. B.2a. The quality of the modal properties extracted with the nonlinear-mode-based method can be assessed by using the identified single-nonlinear-mode model to synthesize the frequency response and compare it against the direct measurements. The results are also depicted in Fig. B.2a. Overall, the synthesized results are in good agreement with the measured reference, confirming the high quality of the extracted modal properties. Moreover, both identification methods agree reasonably with respect to the damping ratio. Finally, for small amplitudes, natural frequency and damping ratio are close to the results obtained by Impact Hammer Modal Testing.

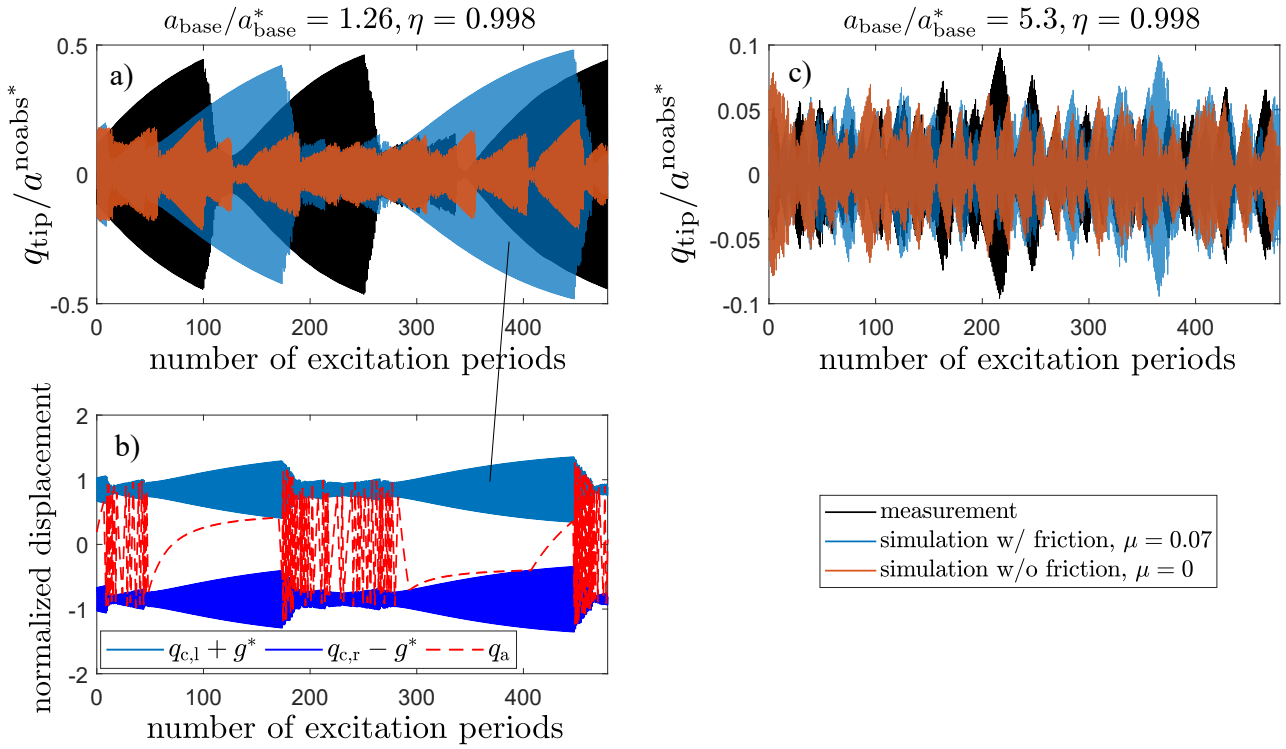


**Fig. C.1:** Influence of dry friction on representative time histories of strongly modulated response: (a) tip response at low excitation level $a_{\mathrm{base}}/a^*_{\mathrm{base}} = 1.26$, (b) corresponding movement of left/right cavity walls and IES, (c) tip response at intermediate excitation level $a_{\mathrm{base}}/a^*_{\mathrm{base}} = 5.3$. $q_{\mathrm{c,l}}, q_{\mathrm{c,r}}$ denote displacement of left and right cavity wall, $q_{\mathrm{a}}$ is the displacement of the IES. All displacements displayed in (b) are normalized with $a^{\mathrm{noabs}^*}$.

The natural frequency shift amounts to about $0.1\%$ and the modal damping ratio increases from about $0.06\%$ to about $0.095\%$ in the considered amplitude range. In the subsequent investigation of the system with IES, it was found that the amplitude range of primary interest, namely the resonant tip response level in the almost periodic regime with two impacts per period, is between $0.58$ mm and $0.95$ mm. In this range, the identified modal damping ratio varies only between $0.075\%$ and $0.09\%$. Thus, both modal properties are fairly constant in the relevant amplitude range, and the system behaves linearly in good approximation. This justifies to simply model the host structure without IES as linear in the subsequent numerical investigations. As nominal value of the modal damping ratio, we use $0.085\%$. The nominal value and the uncertainty bounds of the modal damping ratio are summarized in Tab. 2.
It is interesting to relate the normalized results in Fig. 6 to the non-normalized results in the linearity-check Fig. B.2. This can be easily done by noting that

$$a = \frac{a}{a^{\mathrm{noabs}^*}} \frac{a_{\mathrm{base}}}{a^*_{\mathrm{base}}} \frac{\varphi_{\mathrm{tip}}}{\varphi_{\mathrm{c}}} g^* \,. \tag{B.1}$$

The measurement location is about $12$ mm below the contact location so that $\varphi_{\mathrm{tip}}/\varphi_{\mathrm{c}} \approx 0.96$. Thus, to reconstruct the actual response level $a$, one has to multiply the normalized values on both axes in Fig. 6, and multiply the result by $0.96 \cdot g^* = 0.56$ mm (Tab. 2).

# C Influence of dry friction at low excitation levels

The purpose of this subsection is to demonstrate that dry friction is a plausible explanation for the discrepancy of simulation and measurement at low excitation level. Representative time histories of the steady-state, strongly modulated response are shown in Fig. C.3 at low and intermediate excitation level. At low excitation level, the measured modulation cycles are longer and deeper than at intermediate excitation level. In the experiment, it was observed that the IES comes to a complete rest in certain time spans for low excitation level. This is attributed to dry friction between the lower cavity wall and the IES. Apparently, the acceleration/deceleration due to the dry friction forces is not negligible at sufficiently low excitation (and thus tip acceleration) level. To analyze this hypothesis, the

model of the IES was upgraded by a simple elastic dry friction element (stiffness $22\ \mathrm{kN/mm}$, friction coefficient $0.07$). The tangential contact stiffness was selected in accordance with Cattaneo-Mindlin theory (spherical-on-flat elastic half space, normal load due to gravity), see e. g. [41]. The friction coefficient is an intermediate value between the typical values for the given contact properties under sliding friction ($0.2 - 0.5$ [46]) and rolling friction ($0.001 - 0.002$ [47, 48]). Nevertheless, the sphere is still considered to slide without rolling in the model.
The upgraded model is able to reproduce the long and deep modulation cycles seen in Fig. C.3a. The corresponding movement of the IES between the cavity walls is illustrated in Fig. C.3b. Apparently, friction decelerates the sphere so that it comes to a complete rest, until the vibrations have grown sufficiently to trigger recurrent impacts. From Fig. C.3c, one can infer that friction is much less relevant at higher excitation level. Note that an exact agreement of the simulation with and without friction in Fig. C.3 cannot be expected due to the chaotic character of the vibration.
With the knowledge on the influence of friction, we briefly revisit Fig. 5a-b in order to explain a detail in the measured response. At the lowest 3 and the highest 1-2 excitation frequencies, the measured maximum and mean response levels are almost identical and match well the quasi-linear response without IES. This can now be explained by the IES coming to a complete rest and thus being inactive slightly away from resonance. In contrast, friction is neglected in the simulation and thus the IES remains active.

# D Number of significant impacts per period and the modal coefficient of restitution

To observe the collision events and the motion of the IES within the cavity, high-speed digital image correlation seems ideal, as proposed in [49]. For the present work, however, this facility was not available. Instead the collision events were detected from acceleration signals close to the cavity walls and the motion of the IES was reconstructed assuming frictionless sliding between the cavity walls. This procedure is described in the following subsection. Subsequently, experimental results for the significant impacts per period and the modal coefficient of restitution are shown and confronted with numerical predictions.

## D.1 Impact detection from measured acceleration signals

As illustrated in Fig. 2a-b, the host structure is equipped with an acceleration sensor close to the impact point of each cavity wall. The collisions lead to spikes in the measured acceleration (Fig. D.4a,c). A strong collision leads to a significant spike observable with both sensors, but the spike is more intense when the collision occurs at the respective wall to which the sensor is attached. This permits to detect the time of impact and to associate the impact to the respective wall. The displacement of the cavity walls can be approximated by integrating the respective acceleration. Assuming frictionless sliding, the IES has constant velocity between the impacts. With this, the motion of the IES can

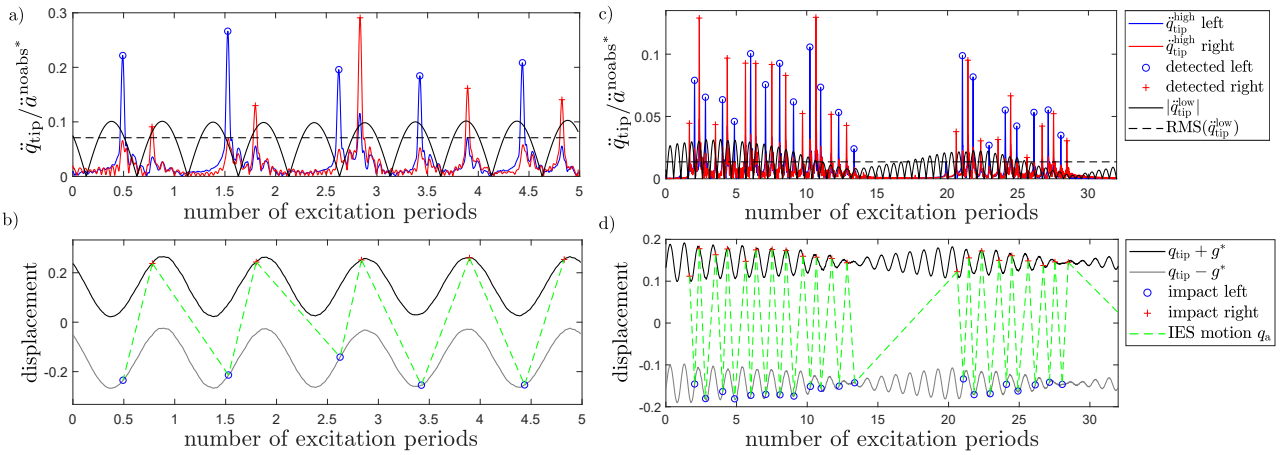


**Fig. D.1:** Illustration of the impact detection and motion reconstruction procedure: (a),(c) representative time history of acceleration near left and right cavity wall; (b),(d) corresponding tip displacement and reconstructed motion of the IES. (a)-(b) correspond to an almost periodic, (c)-(d) to a strongly modulated response. $\ddot{a}^{\mathrm{noabs}^*}$ used for normalization in (a),(c) is defined as $\ddot{a}^{\mathrm{noabs}^*} = \omega^{*2} a^{\mathrm{noabs}^*}$. All displacements displayed in (b),(d) are normalized with $a^{\mathrm{noabs}^*}$.

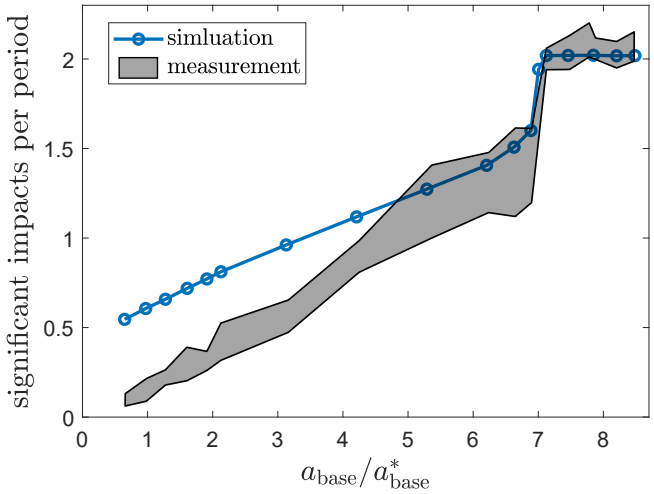


**Fig. D.2:** Average number of significant impacts per excitation period. The spread in the measurement results accounts for the variation of the threshold for impact detection ($80\%$ to $100\%$ of root-mean-square of low-pass filtered tip acceleration).

be completely reconstructed (Fig. D.4b,d).
The signal processing of the acceleration for impact detection can be summarized in the following algorithm:

1. The measured acceleration near the impact point is high-pass filtered (cut-off frequency $20\ \mathrm{kHz}$, slightly higher than the frequency of the highest relevant bending mode).
2. The envelope of this signal is determined.
3. The peaks of this envelope are determined.
4. Peaks with magnitude smaller than the specified threshold are discarded.

The described procedure performed reasonably well in wide ranges. Obviously, a crucial parameter is the threshold. As nominal threshold, we used the root-mean-square value of the low-pass filtered (cut-off frequency $120\ \mathrm{Hz}$, slightly above the frequency of the resonant mode) tip acceleration. This is believed to be a reasonable measure for the vibration level. Of course, if the threshold is too large, less intense collisions will not be detected, which may lead to an inconsistency and thus to failure of the motion reconstruction. If it is too small, spurious impacts are detected, which may also lead to inconsistencies. Time spans of the steady-state response, in which the motion reconstruction failed, are ignored in the following analysis.

## D.2 Validation of significant impacts per period and modal coefficient of restitution

Using the procedure described above, the average number of significant impacts per excitation period can be determined. A considerable sensitivity of the experimental results to the impact detection threshold was observed, especially in the strongly modulated response regime. To account for this uncertainty, the threshold was varied between $80\%$ and $100\%$ of its nominal value (root-mean-square of low-pass filtered tip acceleration). Of course, the higher the threshold, the lower the number of detected impacts. The results are shown as spread (shaded area) in Fig. D.5. The experimental results are compared to the simulation results, which are obtained for nominal parameters $D^*, g^*, k^*_{\mathrm{H}}$ and averaged over multiple simulations as explained in Sect. 5.1. In the simulations, the significant impacts are defined as described in [50]. The comparison in Fig. D.5 reveals a good agreement for high and intermediate excitation levels associated with almost periodic and strongly modulated response, respectively. For low excitation levels, fewer impacts occur in the experiment. As in Appendix C, this is attributed to friction (not modeled). Overall, the results are in good agreement, especially near the optimum, which gives further confidence in the prediction approach.
The *modal coefficient of restitution*, $r$, is defined as

$$r = -\frac{\left[\dot{q}_{\mathrm{tip,mod}} - \dot{q}_{\mathrm{a}}\right]_{t_{\mathrm{c}}^+}}{\left[\dot{q}_{\mathrm{tip,mod}} - \dot{q}_{\mathrm{a}}\right]_{t_{\mathrm{c}}^-}}, \tag{D.1}$$

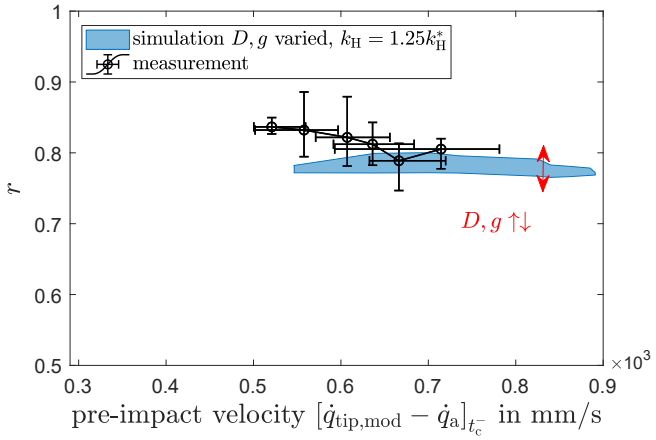


**Fig. D.3:** Modal coefficient of restitution determined for the almost periodic response regime with two impacts per period. The spread in the simulation results corresponds to the variation of $D$ and $g$ as in Fig. 8.

where $t_{\mathrm{c}}^-$ and $t_{\mathrm{c}}^+$ are the time instants before and after an impact, and $\dot{q}_{\mathrm{tip,mod}}$ is the velocity induced only by the fundamental harmonic of the resonant mode. A coefficient of restitution $r < 1$ states that the magnitude of the relative velocities is decreased by the impact, which corresponds to a loss of momentum, and thus mechanical energy, on the slow time scale (of the low-frequency resonant mode). The purpose of the IES is to transfer this mechanical energy irreversibly from the host structure's resonant mode to the off-resonant modes. Therefore, the modal coefficient of restitution is a key parameter in the design of the IES [14]. $r$ can be estimated from the reconstructed motion of the IES and the motion of the cavity walls. To determine $\dot{q}_{\mathrm{tip,mod}}$, the fundamental harmonic of $\dot{q}_{\mathrm{tip}}$ is extracted. For simplicity, it is assumed that the fundamental harmonic of $\dot{q}_{\mathrm{tip}}$ is dominated by the resonant mode. This simplification was verified by the simulation results. The estimated values are averaged over $50$ excitation periods, both in the case of the simulation and the experiment. The results are depicted in Fig. D.6. The good agreement between the measurement and simulation (impact modeled as purely elastic) is a further confirmation that the impact-induced loss of mechanical energy must be mainly due to irreversible scattering to off-resonant modes.

# References

[1] A. F. Vakakis, O. V. Gendelman, G. Kerschen, L. A. Bergman, D. M. McFarland, et al. *Nonlinear Targeted Energy Transfer in Mechanical and Structural Systems*. Springer Berlin Heidelberg, 2008. ISBN 1402091303.

[2] A. L. Paget. Vibration in steam turbine buckets and damping by impacts. *Engineering*, 143:305–307, 1937.

[3] C.-H. Lamarque, O. V. Gendelman, A. Ture Savadkoohi, and E. Etcheverria. Targeted energy transfer in mechanical systems by means of non-smooth nonlinear energy sink. *Acta Mechanica*, 221(1):175, 2011. doi:10.1007/s00707-011-0492-0.

[4] O. V. Gendelman. Analytic treatment of a system with a vibro-impact nonlinear energy sink. *Journal of Sound and Vibration*, 331(21):4599–4608, 2012. doi:10.1016/j.jsv.2012.05.021.

[5] S. F. Masri and T. K. Caughey. On the stability of the impact damper. *Journal of Applied Mechanics*, 33(3):586–592, 1966. doi:10.1115/1.3625125.

[6] C. N. Bapat and S. Sankar. Single unit impact damper in free and forced vibration. *Journal of Sound and Vibration*, 99(1): 85–94, 1985. doi:10.1016/0022-460X(85)90446-8.

[7] P. Lieber, D. P. Jensen, et al. An acceleration damper: development, design and some applications. *Trans. ASME*, 67(10): 523–530, 1945.

[8] M. R. Duncan, C. R. Wassgren, and C. M. Krousgrill. The damping performance of a single particle impact damper. *Vibro-Impact Systems*, 286(1):123–144, 2005. ISSN 0022-460X. doi:10.1016/j.jsv.2004.09.028.

[9] E. Gourc, G. Michon, S. Seguy, and A. Berlioz. Targeted energy transfer under harmonic forcing with a vibro-impact nonlinear energy sink: Analytical and experimental developments. *Journal of Vibration and Acoustics*, 137(3):031008–031008–7, 2015. doi:10.1115/1.4029285.

[10] E. Gourc, S. Seguy, G. Michon, A. Berlioz, and B. P. Mann. Quenching chatter instability in turning process with a vibro-impact nonlinear energy sink. *Journal of Sound and Vibration*, 355:392–406, 2015. doi:10.1016/j.jsv.2015.06.025.

[11] T. Li, E. Gourc, S. Seguy, and A. Berlioz. Dynamics of two vibro-impact nonlinear energy sinks in parallel under periodic and transient excitations. *International Journal of Non-Linear Mechanics*, 90:100–110, 2017. doi:10.1016/j.ijnonlinmec.2017.01.010.

[12] M. A. Al-Shudeifat, A. F. Vakakis, and L. A. Bergman. Shock mitigation by means of low- to high-frequency nonlinear targeted energy transfers in a large-scale structure. *Journal of Computational and Nonlinear Dynamics*, 11(2):1–11, 2015.

[13] T. Theurich, J. Gross, and M. Krack. Effects of modal energy scattering and friction on the resonance mitigation with an impact absorber. *Journal of Sound and Vibration*, 442:71–89, 2019. doi:10.1016/j.jsv.2018.10.055.

[14] T. Theurich, A. F. Vakakis, and M. Krack. Predictive design of impact absorbers for mitigating resonances of flexible structures using a semi-analytical approach. *Journal of Sound and Vibration*, (516):17pp, 2022.

[15] K. P. Duffy, R. L. Bagley, and O. Mehmed, editors. *On a self-tuning impact vibration damper for rotating turbomachinery*, 2000.

[16] T. Li, S. Seguy, and A. Berlioz. On the dynamics around targeted energy transfer for vibro-impact nonlinear energy sink, 01.01.2016.

[17] T. Li, S. Seguy, and A. Berlioz. Optimization mechanism of targeted energy transfer with vibro-impact energy sink under periodic and transient excitation. *Nonlinear Dynamics*, pages 1–19, 2016. doi:10.1007/s11071-016-3200-8.

[18] T. Li, S. Seguy, and A. Berlioz. Dynamics of cubic and vibro-impact nonlinear energy sink: Analytical, numerical, and experimental analysis. *Journal of Vibration and Acoustics*, 138(3), 2016. doi:10.1115/1.4032725.

[19] G. Pennisi, C. Stephan, E. Gourc, and G. Michon. Experimental investigation and analytical description of a vibro-impact nes coupled to a single-degree-of-freedom linear oscillator harmonically forced. *Nonlinear Dynamics*, 88(3):1769–1784, 2017. doi:10.1007/s11071-017-3344-1.

[20] T. Li, D. Qiu, S. Seguy, and A. Berlioz. Activation characteristic of a vibro-impact energy sink and its application to chatter control in turning. *Vibro-Impact Systems*, 405:1–18, 2017. ISSN 0022-460X. doi:10.1016/j.jsv.2017.05.033.

[21] T. Li, C.-H. Lamarque, S. Seguy, and A. Berlioz. Chaotic characteristic of a linear oscillator coupled with vibro-impact nonlinear energy sink. *Nonlinear Dynamics*, 91(4):2319–2330, 2018. doi:10.1007/s11071-017-4015-y.

[22] D. Qiu, S. Seguy, and M. Paredes. Design criteria for optimally tuned vibro-impact nonlinear energy sink. *Vibro-Impact Systems*, 442:497–513, 2019. ISSN 0022-460X. doi:10.1016/j.jsv.2018.11.021.

[23] K. Li and A. P. Darby. An experimental investigation into the use of a buffered impact damper. *Journal of Sound and Vibration*, 291(3-5):844–860, 2006. doi:10.1016/j.jsv.2005.06.043.

[24] K. Li and A. P. Darby. A buffered impact damper for multi-degree-of-freedom structural control. *Earthquake Engineering & Structural Dynamics*, 37(13):1491–1510, 2008. ISSN 0098-8847. doi:10.1002/eqe.823.

[25] W. Yang, Y. Seong, S. Jeong, and J. Park. Vibration reduction using meta-structures composed of tuned dynamic absorbers employing mass impacts. *Composite Structures*, 183(1):216–220, 2017. doi:10.1016/j.compstruct.2017.02.083.

[26] R. K. Roy, R. D. Rocke, and J. E. Foster. Application of impact dampers to continuous systems. *American Society of Mechanical Engineers (Paper)*, (75 -DET-81):1317–1324, 1975. ISSN 04021215.

[27] R. Chalmers and S. E. Semercigil. Impact damping the second mode of a cantilevered beam. *Journal of Sound and Vibration*, 146(1):157–161, 1991. doi:10.1016/0022-460X(91)90528-R.

[28] Butt Aamir S. and Akl Fred A. Experimental analysis of impact-damped flexible beams. *Journal of Engineering Mechanics*, 123(4):376–383, 1997. doi:10.1061/(ASCE)0733-9399(1997)123:4(376).

[29] J. Cheng and H. Xu. Inner mass impact damper for attenuating structure vibration. *International Journal of Solids and Structures*, 43(17):5355–5369, 2006. doi:10.1016/j.ijsolstr.2005.07.026.

[30] R. Vinayaravi, D. Kumaresan, K. Jayaraj, A. K. Asraff, and R. Muthukumar. Experimental investigation and theoretical modelling of an impact damper. *Vibro-Impact Systems*, 332(5):1324–1334, 2013. ISSN 0022-460X. doi:10.1016/j.jsv.2012.10.032.

[31] Y. Yang, L. Jézéquel, O. Dessombz, P. Bristiel, and O. Sauvage. Modelization of boundary friction damping induced by second-order bending strain. *Journal of Sound and Vibration*, 446:113–128, 2019. doi:10.1016/j.jsv.2019.01.033.

[32] R. Chabrier, G. Chevallier, E. Foltête, and E. Sadoulet-Reboul. Experimental investigations of a vibro-impact absorber attached to a continuous structure. *Mechanical Systems and Signal Processing*, 180:109382, 2022. doi:10.1016/j.ymssp.2022.109382.

[33] M. Scheel, G. Kleyman, A. Tatar, M. R. Brake, S. Peter, et al. Experimental assessment of polynomial nonlinear state-space and nonlinear-mode models for near-resonant vibrations. *Mechanical Systems and Signal Processing*, 143, 2020, URL https://doi.org/10.1016/j.ymssp.2020.106796.

[34] G. Dhondt and K. Wittig. Calculix: a free software three-dimensional structural finite element program. www.calculix.de, 1998.

[35] F. Moser, L. J. Jacobs, and J. Qu. Modeling elastic wave propagation in waveguides with the finite element method. *NDT & E International*, 32(4):225–234, 1999. ISSN 0963-8695.

[36] M. Géradin and D. J. Rixen. *Mechanical vibrations: theory and application to structural dynamics*. John Wiley & Sons, 2014.

[37] T. Li, S. Seguy, C.-H. Lamarque, and A. Berlioz. Experiment-based motion reconstruction and restitution coefficient estimation of a vibro-impact system. *Journal of Vibration and Acoustics*, 141(2), 2018. doi:10.1115/1.4041367.

[38] W. Goldsmith. *Impact*. Courier Corporation, 2001. ISBN 0486420043.

[39] R. Seifried, W. Schiehlen, and P. Eberhard. Numerical and experimental evaluation of the coefficient of restitution for repeated impacts. *Fifth International Symposium on Impact Engineering*, 32(1):508–524, 2005. ISSN 0734-743X. doi:10.1016/j.ijimpeng.2005.01.001.

[40] F. Gehr, T. Theurich, J. Gross, S. Schwarz, A. Hartung, et al. Computational and experimental analysis of the impact of a sphere on a beam and the resulting modal energy distribution. *Mechanical Systems and Signal Processing*, (submitted).

[41] K. L. Johnson. *Contact Mechanics*. Cambridge University Press, Cambridge, 1989. ISBN 0-521-25576-7.

[42] K. Willner. Fully coupled frictional contact using elastic halfspace theory. *Journal of Tribology*, 130(3), 2008. ISSN 0742-4787. doi:10.1115/1.2913537.

[43] R. Jankowski. Analytical expression between the impact damping ratio and the coefficient of restitution in the non-linear viscoelastic model of structural pounding. *Earthquake engineering & structural dynamics*, 35(4):517–524, 2006.

[44] D. J. Ewins. *Modal Testing: Theory and Practice*. Research Studies Press Ltd., Taunton, 1995.

[45] C. Gibert. Fitting measured frequency response using non-linear modes. *Mechanical Systems and Signal Processing*, 17(1): 211–218, 2003. doi:10.1006/mssp.2002.1562.

[46] J. R. Davis. *Concise metals engineering data book*. ASM international, 1997.

[47] F. Sass, C. Bouché, and A. Leitner. *Dubbels Taschenbuch für den Maschinenbau: Bearb v.(fl. forf.)*. Springer, 1966.

[48] L. Minkin and D. Sikes. Coefficient of rolling friction-lab experiment. *American Journal of Physics*, 86(1):77–78, 2018.

[49] R. Chabrier, E. Sadoulet-Reboul, G. Chevallier, E. Foltête, and T. Jeannin. Full-field measurements with digital image correlation for vibro-impact characterisation. *Mechanical Systems and Signal Processing*, 156:107658, 2021. doi:10.1016/j.ymssp.2021.107658.

[50] B. Fang, T. Theurich, M. Krack, L. A. Bergman, and A. F. Vakakis. Vibration suppression and modal energy transfers in a linear beam with attached vibro-impact nonlinear energy sinks. *Communications in Nonlinear Science and Numerical Simulation*, 91:105415, 2020. ISSN 1007-5704. doi:10.1016/j.cnsns.2020.105415.